Three-dimensional induced polarization data inversion for complex resistivity

Michael Commer[1], Gregory A. Newman[1], Kenneth H. Williams[1], and Susan S. Hubbard[1]

[1]Lawrence Berkeley National Laboratory, Earth Sciences Division, Berkeley, California

Abstract

The conductive and capacitive material properties of the subsurface can be quantified through the frequency-dependent complex resistivity. However, the routine three-dimensional interpretation of voluminous induced polarization (IP) data sets still poses a challenge due to large computational demands and solution non-uniqueness. In this work, we propose a flexible methodology for three-dimensional (spectral) IP data inversion. Our inversion algorithm is adapted from a frequency-domain electromagnetic (EM) inversion method primarily developed for large-scale hydrocarbon and geothermal energy exploration purposes. The method has proven to be efficient by implementing the non-linear conjugate gradient method with hierarchical parallelism and by using an optimal finite-difference forward modeling mesh design scheme. The method allows for a large range of survey scales, providing a tool for both exploration and environmental applications. We experiment with an image focusing technique in order to improve the poor depth resolution of surface data sets with small survey spreads. The algorithm's underlying forward modeling operator properly accounts for EM coupling effects, thus traditionally used EM coupling correction procedures are not needed. The methodology is applied to both synthetic and field data. The benefit of directly inverting EM coupling contaminated data is demonstrated on a synthetic large-scale exploration data set. Afterwards, we demonstrate the monitoring capability of our method by inverting time-lapse data from an environmental remediation experiment near Rifle, Colorado. Similar trends observed in both our solution and another two-dimensional inversion are in accordance with previous findings about the IP effects due to subsurface microbial activity.

Introduction

The induced polarization (IP) method was originally developed for mineral prospecting of iron-sulfide (FeS) formations because of strong polarization phenomena at the interface between metallic minerals and pore fluids (e.g., Sumi, 1959; Madden and Cantwell, 1967; Van Voorhis et al., 1973; Pelton et al., 1978). For a large class of sulfide deposits and other mineral types that represent electronic conductors, for example magnetite and graphite, the IP method provides a strong indicator. The use of the IP effect to predict hydraulic properties (e.g., Vacquier et al.,

1957) is more indirect and thus ambiguous than in sulfide mineral exploration. Therefore, only recently, i.e. during the last decade, has the IP method gained popularity in field-scale environmental and engineering applications. Utilized is the sensitivity to lithologic parameter changes, such as hydraulic conductivity, surface area, and grain size (Börner et al., 1996; Slater and Lesmes, 2002), as well as to pore solution chemistry and microscopic structure (Kemna et al., 2000; Hördt et al., 2007; Williams et al., 2009). The ambiguity in interpreting IP effects stems from different types of polarization effects which furthermore exhibit a frequency-dependence. We refer the reader to a recent work by Revil and Florsch (2010) for a comprehensive research overview of the governing mechanisms and the related efforts of other authors. Recent works indicate that the main IP contribution related to hydraulic parameters, in the absence of metallic minerals, comes from polarization of ions within the Stern layer, the inner portion of the electrical double layer coating the surface of the minerals (Revil and Florsch, 2010, and references therein).

Utilizing the frequency dependence of polarization mechanisms increases the informative value of IP data by additional phase lag information, measured between a voltage sinusoid and an impressed current sinusoid. Spectral IP (SIP) responses are a complex function of pore solution chemistry, surface chemical properties, and microscopic structure. Finding one macroscopic parameter for these properties, which describes both conductive and capacitive properties of a material, leads to the complex electrical conductivity (σ^*), or the reciprocal (ρ^*), the complex resistivity (CR). Expressed in terms of a magnitude and phase, or by real and imaginary parts, one has (i=imaginary unit)

$$\sigma^* = |\sigma| e^{i\theta} = \sigma^r + i\sigma^q.$$

The real component σ^r represents current flow in phase with the injected source field. The imaginary (also referred to as quadrature) conductivity σ^q is one of the commonly used normalized IP parameters and is derived from the field IP parameter phase, θ, by $\sigma^q = \sigma^r \tan(\theta)$. The imaginary conductivity relates to the current component out of phase by 90 degrees with the source current.

Most related studies about physiochemical parameters controlling complex conductivity responses of rocks and soils have been performed at the laboratory scale (Börner et al., 1996;

Ulrich and Slater, 2004; Williams et al., 2005). Field-scale surface SIP measurements for complex tasks such as monitoring biogeochemical processes have only recently been utilized (Williams et al., 2009). Challenges are given by geologically complex situations and time variant parameter changes. Owing to these complexities, it has been understood that it is important to take the three-dimensionality of the Earth into account in order to minimize the errors introduced by assuming one- or two-dimensional models. Despite a lot of recent progress in the field of surface IP data acquisition and inversion (Kemna and Binley, 1996; Kemna et al., 2000, Weller et al., 2000; Loke et al., 2006), key problems remain to be the typically large computing demands of 3-D inversions and the non-uniqueness problem given by the highly parameterized 3-D models.

Most inversion algorithms for IP data have underlying forward solutions that assume negligibly small inductive effects (Oldenburg and Li, 1994; Shi et al., 1998; Yang and LaBreque, 2000; Kemna, 2000). These approaches imply sufficiently low measurement frequencies. Higher frequencies, as well as higher conductivities and larger transmitter-receiver electrode separations, introduce an inductive component which is superimposed on the IP effect of interest and is referred to as electromagnetic (EM) coupling. In general, for two electrode circuits at the Earth's surface, their mutual impedance Z as a function of angular frequency ω is defined as the ratio $Z(\omega)=U_2(\omega)/I_1(\omega)$, where U_2 refers to the voltage in the secondary circuit (potential electrodes), and I_1 refers to the alternating current in the primary circuit (current electrodes). $Z(\omega)$ consists of a CR contribution owing to the Earth's polarization, the desired signal, and an induced coupling component between the primary and secondary circuits. Traditional approaches treat the inductive portion of IP measurements as noise, and hence its removal may be a loss of useful information. Furthermore, the removal necessitates additional data processing steps. Much effort has been put into the development of algorithms, involving both empirical and physics-based models, that separate inductive coupling responses from CR observations (e.g., Wynn and Zonge, 1975; Song, 1984; Routh and Oldenburg, 2001; Ingeman-Nielsen and Baumgartner, 2006). An alternative demonstrated in this work consists of incorporating EM coupling directly into SIP data simulations at the expense of higher computational costs.

The present study aims at further advancing the methodological framework available for interpreting field-scale SIP measurements. We have adapted a finite-difference (FD) imaging

algorithm for controlled-source EM data, introduced in an earlier work (Commer and Newman, 2008), to handle 3-D SIP data inversion. A hierarchical parallel implementation (Commer et al., 2008) addresses the large computing demands and makes efficient use of multi-processor computers as they are becoming more common for scientific applications. The algorithm further features a computationally efficient grid separation scheme, which allows the design of optimized FD grids for accelerated forward modeling solutions. The underlying forward operators can be chosen to either solve the full Maxwell equations or the Poisson equation for complex conductivity which covers a broad range of applications. Treating Maxwell's equations in the forward problem enables the inversion of SIP data for complex resistivity taking EM coupling effects into account.

After briefly introducing the forward and inverse modeling framework, we introduce a method of vertical resolution enhancement using a depth weighting scheme. Depth weighting functions have for example been applied successfully to inverse problems for static potential field data (Li and Oldenburg, 1998). In the present work we experiment with applying both depth and lateral weighting directly to the gradient of the inverse solution's objective functional. This method provides a simple way of attenuating the high sensitivities of inversion parameters (in the form of model grid cells) near sensor positions, thus achieving a focusing effect at larger depths. In the following sections, we first demonstrate the benefit of directly inverting EM coupling contaminated data by solving Maxwell's equations in the forward modeling operator. Then, data inversions from the Rifle Integrated Field-Scale Subsurface Research Challenge site (Colorado), a research area for studying the feasibility of bio-stimulated environmental remediation, are presented. The Rifle study examines the image focusing effect of the gradient weighting scheme and further demonstrates the monitoring capability for time-variant complex resistivity anomalies.

Method

The inverse algorithm used in this work involves two methodologies to recover complex conductivity structure from frequency-domain IP data. The first one involves a forward operator which solves the full 3-D Maxwell equations for the electric field, referred to as the EM problem

in the following. This approach, while computationally expensive, accounts for EM coupling effects. The second forward modeling operator solves the Poisson equation for a complex potential field, referred to as the DC problem. Although the latter is formally equivalent to solutions to conventional DC resistivity problems, the frequency dependence enters the equation through the complex conductivity. Since EM coupling effects are neglected, this approach is only appropriate when frequencies approach the static limit. Both methods will be applied to imaging problems shown further below.

Only isotropic complex conductivity models will be studied below. However, with the underlying material averaging scheme of the forward modeling operator, outlined in detail in an earlier work (Commer and Newman, 2008), an anisotropic formulation of the forward problem falls in place (Newman et al., 2010). Therefore, our method also allows simulating fields from an anisotropic complex conductivity distribution.

Forward solution using Maxwell's equations

The inversion approach presented here involves a forward solution of the full 3-D Maxwell equations for the electric field. Solving Maxwell's equation in the quasi-static limit for the vector electric field, **E**, one has (Newman and Alumbaugh, 2002)

$$\nabla \times \nabla \times \mathbf{E} + i\omega\mu_0\sigma^*\mathbf{E} = -i\omega\mu_0\mathbf{J}. \tag{1}$$

In this formulation, μ_0 and $\omega = 2\pi f$ denote the free-space magnetic permeability and angular frequency, where f is measured in Hz. The complex conductivity is given by the tensor

$$\sigma^* = \begin{pmatrix} \sigma^*_{xx} & 0 & 0 \\ 0 & \sigma^*_{yy} & 0 \\ 0 & 0 & \sigma^*_{zz} \end{pmatrix},$$

where σ^*_{xx}, σ^*_{yy}, and σ^*_{zz} denote the directional complex conductivities along the three Cartesian coordinates. We define the forward problem as a scattered field formulation for Maxwell's equations, where the total electric field is given by the sum of a background and scattered electric field, $\mathbf{E} = \mathbf{E}_b + \mathbf{E}_s$. In this case, the source vector **J** is written as

$$\mathbf{J} = (\sigma^* - \sigma^*_b)\mathbf{E}_b,$$

where $\bar{\sigma}_b$ is the background's complex conductivity tensor, and $\mathbf{E}_b$ is the corresponding electric field. Because of computational efficiencies, it is common to use half-space or layered (one-dimensional) background models, for which analytical field solutions exist. The scattered field formulation is the preferred way in well-logging applications because of the fact that measurements are usually close to the source (Newman and Alumbaugh, 2002). Scattered fields have a smoother spatial dependence when source positions are located in the vicinity of anomalous conductivities. In the surface case presented here, the electrode configuration covers only a few tens of meters and thus the same reason applies for using a scattered field solution. Equation 1 is solved in three dimensions using a FD formulation. Discretizing equation 1 on a staggered FD grid leads to the linear system

$$\mathbf{K}_{EM}\mathbf{E}_s = \mathbf{S}_{EM}, \tag{2}$$

which is complex symmetric and sparse with 13 non-zero entries per row (Newman and Alumbaugh, 2002). The right hand side $\mathbf{S}_{EM}$ is a discrete scaled representation of the right hand side of equation 1, where one solves for the scattered electric field. We use the QMR (quasi-minimum residual) method with Jacobi preconditioning for solving the system. For computational efficiency, the system is solved on distributed computer systems, using the message passing interface (MPI). This is realized by using a FD grid decomposition within a MPI communicator with Cartesian topology. Within this communicator, each parallel task is assigned to a subcube of the 3D mesh underlying equation 2. At another over-arching level, an arbitrarily high number of forward problems can be distributed over a designated number of Cartesian solution communicators (Commer et al., 2008).

A limitation to solving the forward modeling problem of equation 2 is the fact that the system becomes increasingly ill-conditioned as frequencies approach the static limit. To address this problem, a class of additional preconditioners has been proposed, which are based on a Helmholtz decomposition of the electric field in the low induction number regime. We refer to the work of Newman and Alumbaugh (2002) and references therein for an implementation of the low induction number preconditioner. This preconditioner type was used for all shown imaging results which solve equation 2 in the forward operator.

Forward solution using Poisson's equation

Without frequency dependence, the electric field is curl-free and thus can be written as $\mathbf{E} = \nabla\varphi$, where φ is a scalar complex potential. The potential field is obtained through solution of the Poisson equation,

$$\nabla \cdot (\sigma^* \nabla \varphi) = \nabla \cdot \mathbf{J}, \tag{3}$$

where **J** represents the DC source current distribution. Owing to similar reasons as mentioned above, we also employ a scattered field version for the results shown in this work, realized by solving the equation

$$\nabla \cdot (\sigma^* \nabla \varphi_s) - \nabla \cdot \left[(\sigma^* - \sigma_b^*) \nabla \varphi_b \right]. \tag{4}$$

The resulting complex matrix system

$$\mathbf{K}_{DC} \varphi_s = \mathbf{S}_{DC} \tag{5}$$

is solved for the (scattered) complex potential field φ_s via a generalized bi-conjugate gradient solver. The scattered field formulation for the potential field utilizes the above mentioned background one-dimensional electric fields, $\mathbf{E}_b = -\nabla\varphi_b$, calculated from the background conductivity distribution σ_b^*.

Inverse solution

A detailed formulation of the EM inverse solution as it is used for the present study is given in an earlier work (Commer and Newman, 2008, and references therein). Here, we outline the basic methodology relevant to treating complex conductivity parameters. The SIP inverse problem is formulated by means of an error function to be minimized,

$$\phi = \phi_d + \phi_m = \frac{1}{2}[\mathbf{D}(\mathbf{d}^o - \mathbf{d}^p)]^*[\mathbf{D}(\mathbf{d}^o - \mathbf{d}^p)] + \frac{1}{2}\sum_{i=1}^{s} \lambda_i (\mathbf{W}_i \mathbf{m}_i)^*(\mathbf{W}_i \mathbf{m}_i), \tag{6}$$

where * denotes complex conjugation. The first term on the right hand side (Φ_d) contains the data misfit between the vectors of observed ($\mathbf{d}^o$) and predicted ($\mathbf{d}^p$) data, where the latter is assessed through a model guess, in geophysical inverse problems often also referred to as the starting model. The data vectors have a size of *N* complex data. The measurement errors enter the error functional through the diagonal weighting matrix $\mathbf{D}_{N\times N}$. Minimization of the objective functional is realized by a non-linear conjugate gradient (NLCG) scheme. The initial model guess is iteratively refined during subsequent NLCG iterations.

The second term (Φ_m) of equation 6 regularizes the model roughness, realized by the smoothing matrix $\mathbf{W}_{M\times M}$, where *M* is the number of unknown FD cell parameters in the inverse problem. These parameters are given by the rectangular cells of a 3-D Cartesian FD model grid. In the isotropic case, the total model vector **m** is thus of size 2*M* and consists of the stacked real (*i*=1) and imaginary (*i*=2) components of the grid cell conductivities,

$$\mathbf{m} = (\mathbf{m}_1, \mathbf{m}_2)^T = (\sigma_1^r, \ldots, \sigma_M^r, \sigma_1^q, \ldots, \sigma_M^q)^T \tag{7}$$

To reduce model roughness in three dimensions, **W** is given by a FD approximation of the Laplacian operator and applied to each model vector component $\mathbf{m}_i$. A balance between data misfit minimization and model regularization is achieved by the regularization parameter λ. The model regularization can in principal be chosen to differ between real and quadrature conductivity in order to account for differing orders of magnitude between σ^r and σ^q. A typical approach for proper selection of λ consists of a cooling approach (Newman and Alumbaugh, 2002) where one decreases λ successively during the course of several inversion runs until a target misfit is achieved. Extended to complex conductivity, a rigorous approach would involve two cooling approaches for both σ^r and σ^q, where the other one is fixed. However, all synthetic studies shown below used $\lambda_1 = \lambda_2 = \lambda = 1$ and provided satisfactory inversion results. Hence, $\lambda = 1$ was also chosen for the field data inversions.

In addition to the above mentioned hierarchical parallelization scheme, we achieve additional computational efficiencies by using an optimized grid scheme (Commer and Newman, 2008). In principal, the scheme allows for computing the forward solution on a FD grid which can be independent of the grid defining the model parameter space defining the electrical conductivity distribution. Both the spatial sampling and size of the meshes used for calculating forward

solutions can then be adapted specifically to the given source frequencies, profile distances, and spatial measurement intervals. The grid separation algorithm involves a proper conductivity averaging scheme which has been outlined in detail for real-valued conductivities. This material averaging scheme applies in the same way for complex conductivities as outlined for the general case of anisotropic conductivities in the appendix. There, we also provide more details about methodological extensions needed for calculating the objective functional gradient $\nabla\phi$ with respect to complex conductivity parameters, generalized for the anisotropic case.

Spatial gradient weighting

A well-known problem in the inversion of geophysical surface measurements is a quickly decaying depth resolution, compared to resolution properties provided by cross-well data. As a result, reconstructed conductivity anomalies may tend to concentrate near the surface. Several aspects aggravate this problem. First, the dipole-dipole configurations typically used in IP measurements do not have strong depth resolution. Moreover, an overestimated contrast between a CR anomaly and its background may result in a smaller than the actual anomaly depth, according to the principle of equivalence (Weller et al., 2000). Finally, not properly balanced model-smoothing constraints can further weaken the reconstruction of structure anomalies at depth. To counteract this behavior, we experiment with applying a 3-D weighting function to the gradient of the objective functional in equation 6. The scheme works as follows: Before entering the NLCG line-search algorithm, the gradient vector is augmented by a weighting function *f* such that the alternated gradient has the form

$$\widetilde{\nabla\phi} = f(x,y,z)\nabla\phi \quad . \tag{8}$$

The weighting function *f* is chosen in a way that the inherently high sensitivities of the model grid cells near the surface, i.e. in the proximity of receiver electrodes, are damped. In principal, the weighting behavior of this function aims at compensating for the fact that the NLCG method is characterized by less aggressive model updating steps compared to Gauss-Newton schemes, the latter typically used, because computationally feasible, in 1-D and 2-D inversion frameworks.

In addition to depth weighting, the scheme also allows to define a lateral focusing volume for the inversion domain. While a variety of weighting functions may be applied in this way, we propose exponential types of weighting functions defined over a 3-D volume. Considering the vertical coordinate, the desired function behavior for surface measurements is in principle to down-weight the gradient vector near the surface (z=0), in our case defining the top of the vertical inversion domain, by a factor a<1. With increasing depth z>0, $f(z)$ shall approach a value of 1 in order to ease the down-weighting behavior. This can be achieved by combining exponential functions to

$$f_1(z) = \frac{a + \exp\left[r\,\frac{(z - z_1)}{dz}\right]}{1 + \exp\left[r\,\frac{(z - z_1)}{dz}\right]}, \tag{9}$$

In our algorithm, the depth range over which $f_1(z)$ changes from a to 1, and thus the steepness of the function increase from a to 1, can be chosen by the value of z_1. The quantity dz is the (vertical) extension of the inversion domain. The behavior of this function is illustrated by the blue curve in Figure 1, where the base weighting is a=0.1 and the steepness of the curve is defined by z_1=5. The vertical inversion domain extends from z=0 m to z=15 m (dz=15 m). Note that $f_1(z = z_1) = \frac{a+1}{2}$. The factor r is an internally calculated scaling factor applied to the exponential arguments which ensures that $f_1(z = 0) \approx a$.

One may further wish to define a focusing inversion domain by $f(z_1a) = a, f(z_1b) = 1, f(z_1c) = a, \quad z_1a < z_1b < z_1c)$. This is achieved by multiplication of f_1 with a second function

$$f_2(z) = \frac{1 + a \cdot \exp\left[r\,\frac{(z - z_2)}{dz}\right]}{1 + \exp\left[r\,\frac{(z - z_2)}{dz}\right]}. \tag{10}$$

This function has a somewhat reversed behavior of f_1. As exemplified in Figure 1 (green curve), the choice of z_2 (note again that $f_2(z = z_2) = \frac{a+1}{2}$) defines the rate at which $f_2(z)$ decreases from $f_2(z) \approx 1$ to a value of a. Combining these two functions yields

$$f(z) = f_1(z) f_2(z) s$$

as shown by the black curve. The factor s is a scaling factor which ensures that the maximum of $f(z)$ is always 1. Such a focusing function behavior is more reasonable along the horizontal coordinates of the inversion domain. Therefore, we combine $f_1(z)$ and $f_2(z)$ with the same sort of function pairs applied to the x and y coordinates, and obtain

$$f(x, y, z) = f_1(x) f_2(x) f_1(y) f_2(y) f_1(z) f_2(z) s. \tag{11}$$

The 3-D gradient weighting behavior of $f(x, y, z)$ is exemplified below. Parameter sensitivities usually decay rapidly with depth. In order to avoid down-weighting the gradient components at larger depths, in $f_2(z)$ we simply set z_2 to an arbitrarily large number. Then $f_2(z) \approx 1$ over the whole vertical imaging domain. In an imaging study below, it is shown how a model sensitivity map may provide guidance for approaching a specific weighting function.

Examples

3-D SIP synthetic data inversion of EM coupling contaminated data

In mining applications SIP measurements have the potential of discriminating mineral types. Mining surveys often deal with large offsets between transmitting and receiving electrodes, thus inductive coupling effects between the wire layouts may become significant (Dey and Morrison, 1973). If not properly accounted for, the inability of not being able to distinguish between IP rock responses and EM coupling effects can distort imaging results, particularly if the IP spectrum is dominated by EM coupling contributions. Extensive studies have been carried out to both simulate and correct for EM coupling effects. To quantify the mutual impedance for dipole-dipole configurations with respect to dipole separation, dipole length, subsurface conductivity, and frequency, a common measure is the percent frequency effect, or PFE (Dey and Morrison, 1973),

$$\mathrm{PFE}_i = \left(1 - \frac{Z_i^{em}}{Z_i^{dc}}\right) \cdot 100\,(\%); \qquad i = 1, \ldots, N,$$

where z_i^{dc} refers to the direct current (low frequency) mutual resistance of the *i*th data point, and z_i^{em} refers to the data point's frequency-dependent mutual resistance, which we calculate using the full EM forward solution (equation 2). Another measure considered will be the corresponding phase difference $\Delta\theta = \theta_i^{em} - \theta_i^{dc}$.

In the following, we demonstrate the necessity of employing the full EM equations in the forward modeling operator when inverting data containing both polarization effects of the subsurface material and significant EM coupling effects. A mineral exploration survey is modeled, with the survey layout with respect to the target anomaly shown in Figure 2. Five dipole-dipole profiles crossing the anomaly are simulated, where a single excitation frequency of 1 Hz is used. Dipole lengths are 100 m and 50 m for transmitters and receivers, respectively. Only receiver dipoles that are in line with the transmitter dipoles are considered. The data set to be inverted hence contains 60 dipole sources and a total of *N*=900 complex data points, contaminated by Gaussian distributed noise with a 3 percent relative magnitude. To have independence from the forward solution employed in the inversion process, the data was generated using a different forward modeling code which uses an integral-equation solution (Newman et al., 1986).

The mineral deposit is given by a conductive (1 S/m) block with dimensions $200\ \mathrm{m} \times 600\ \mathrm{m} \times 100\ \mathrm{m}$ embedded within a more resistive (0.01 S/m = 100 $\Omega \cdot \mathrm{m}$) half-space. Its top boundary is at a depth of 100 m. A complex conductivity of $\sigma^{r} = 1$ S/m and $\sigma^{q} = 0.05$ S/m is assigned to the anomaly and corresponds to a phase of 50 mrad. No phase anomaly is attributed to the background. The EM coupling effect is quantified in Figure 3 for the true model response, showing both PFE and phase difference. Both quantities show an increasing EM coupling effect with increasing transmitter-receiver separation, where the maximum phase difference reaches almost 20 mrad.

Horizontal conductivity transects at depths between *z*=0 m and *z*=300 m, obtained from using the 3-D EM and DC imaging solutions, are compared in Figure 4 (c – f) together with the true model (a – b). Although there are some artifacts in the deep part of the image produced, both geometry and increased conductivity values of the anomaly are clearly indicated by the EM solution (Figure 4, c and d). The DC solution achieves a close reproduction of the deposit's anomalous

conductivity magnitude (or real part of the complex conductivity). However, the imaginary conductivity image appears greatly distorted, indicating that the solution reaches a local minimum. This was also confirmed by the fact that the NLCG algorithm ended prematurely in the line-search procedure after 92 inversion iterations without being able to reach a further objective functional decrease. The inversion run employing the EM forward solution on the other hand was able to proceed to a preset maximum of 500 iterations (Figure 5). The results demonstrate that the significant inductive portion of SIP measurements in this case has to be taken into account.

3-D SIP field data inversion

The time-lapse monitoring capability of the presented inverse solution shall be demonstrated on a field data set. The following 3-D inversions involve data from an environmental remediation monitoring experiment measured at the Integrated Field-Scale Subsurface Research Challenge site at Rifle (Colorado), referred to as Rifle site below. The site has been established by the U.S. Department of Energy to carry out systematic studies of artificially stimulated biogeochemical subsurface processes. Geophysical laboratory experiments proved that sedimentary alterations caused by microbe-mediated sulfide mineral precipitation were concurrent with phase changes (Ntarlagiannis et al., 2005; Williams et al., 2005). Williams et al. (2009) investigated whether the IP method can delineate regions of stimulated (by acetate amendment) iron and sulfate reduction caused by the accumulation of electroactive ions such as Fe(II) and dissolved sulfide. The authors were able to show that fluids and sediments recovered from regions exhibiting an anomalous phase response in IP field measurements showed increased Fe(II) concentrations.

Based on these findings, a number of SIP field measurements have been conducted to investigate the feasibility of monitoring how microorganisms alter their physical and chemical environment during bioremediation on a field scale. Williams et al. (2009) produced SIP inversion results from Rifle data using a finite-element algorithm that solves directly for conductivity magnitude and phase (Kemna, 2000), with the region of interest represented as a 2-D distribution of magnitude and phase values. The 2-D approach has been a legitimate approximation, because, as will be demonstrated in a sensitivity study below, the data are primarily sensitive to conductivity

variations along and beneath the measurement profile, with strongly reduced sensitivity to lateral or broadside variations. In the following, we employ the finite-element method for image comparisons and refer to it as 2-D solution, while our 3-D FD algorithm is referred to as 3-D solution for brevity. The SIP data interpreted in this work were collected in the year 2007. Although it was found that EM induction effects can dominate the IP spectrum above 10 Hz (Kemna et al., 2000), accounting for such effects is neglected, given the frequencies of the data (≤4 Hz). For computational efficiency, we therefore neglect EM coupling and solve the scattered field version of the DC problem (equation 4) for the underlying forward problems.

Environmental remediation monitoring field site and SIP data collection

A comprehensive description of the local geology, hydrology and geochemistry of the Rifle site has been presented by Andersen et al. (2003). The site is located on a flood plain in Northwestern Colorado. The local aquifer is comprised of approximately 6.5 m of unconsolidated sands, silts, clays and gravels deposited by the Colorado River, with the uppermost 2 m being an artificial clay-rich cover. The aquifer is heterogeneous but typical hydraulic conductivities are 7.5 m/day ($\approx 8.7 \cdot 10^{-5}$ m/s). The depth to water table fluctuates seasonally, averaging 3.5 m below ground surface; site groundwater flow direction is predominantly toward the southwest. The local aquifer is contaminated by uranium caused by tailings of a decommissioned uranium mill.

The measurement layout is sketched in Figure 6. Groundwater was pumped from an up-gradient portion of the aquifer into a storage tank and amended with the biostimulating substances acetate and bromide. Ten injection wells, shown in Figure 6, are oriented orthogonal to groundwater flow direction and were used to inject the acetate and bromide into the aquifer over a period of 31 days. In order to monitor geochemical changes resulting from stimulated microbial activity, groundwater samples were collected at 2-5 day intervals from wells down-gradient from the region of stimulant amendment (wells D01-D12 in Figure 6).

Surface SIP data were acquired along two 29 m long transects at five times from August through November 2007. Figure 6 shows the two profiles, also referred to as Array A and B in the following. Table 1 lists the recording times for both arrays. The transects were oriented

perpendicular to groundwater flow direction and located 3 and 9 m down-gradient from the injection well gallery. Data were acquired using a modified dipole-dipole configuration between thirty equally spaced $Cu/CuSO_4$ electrodes, with a dipole spacing of 4 m and a total of 24 potential dipoles per current dipole. Measurements are given by resistance magnitude and phase values and were taken by cycling dipole-dipole configurations through a profile, where for example the first transmitting electrode pair is (1,5), and the receiving pairs are (2,6), (3,7), (4,8), (6,10), …, (26,30). Contact resistance between the electrodes ranged from 600-1000 Ω. All datasets were comprised of reciprocal data pairs, wherein electrodes used to apply current and measure voltage were reversed and data re-acquired. Data were collected using a Zonge GDP-32 recording device at three frequencies (0.125, 1, and 4 Hz) with a Zonge ZT-30 transmitter (55 V; maximum current density of 3 mA/cm^2 = 30 A/m^2). Modeling the data of one measurement day involves solving 52 3-D forward problems (26 transmitter-receiver configurations for each profile).

Since our employed 3-D forward solution generates complex electric field values, we find it preferable to convert the resistance magnitude and phase observations to complex electric field values. The real and imaginary electric field components, E^r and E^q, are obtained from a complex datum d^* consisting of normalized resistance magnitude $|R|$ and the phase θ by (i=imaginary unit)

$$d^* = |R|e^{i\theta} = E^r + iE^q. \tag{12}$$

This approach has two advantages. First, one avoids additional non-linear transformations which would otherwise be introduced into the inverse solution by converting the complex electric field predictions into magnitude and phase values. Second, phase discontinuities between ±π in the data simulations are rather difficult to handle in terms of calculating misfit errors between the observed and simulated data vectors, $\mathbf{d}^o$ and $\mathbf{d}^p$. At last, while the behavior of resistance errors in electrical resistivity imaging is well understood, a thorough analysis of the phase errors is still lacking. Based on the analysis of data sets measured in the frequency range from 1 Hz to 1 kHz, Flores-Orozco et al. (2010) propose an advanced model for the description of phase data errors, which was adapted for the comparative 2-D inversion carried out in this work.

In our 3-D solution, in order to assign proper weights w_i (by means of the weighting matrix **D**) to the complex electric field data, we use the reciprocal measurements. In practice, the errors assigned to each complex datum (E_i^r,E_i^q), are determined using an averaging scheme. The inverted data set, comprising all five recording times and all 52 transmitter-receiver profile configurations, contains 4158 pairs of resistance magnitude and phase data. We chose to discard real electric field measurements with a percentage error, calculated from the reciprocal measurements, larger than 5 percent. This amounts to roughly 4000 real electric field values. A threshold of 10 percent was chosen for the imaginary components. Data pairs with reciprocal differences above these percentage thresholds are given arbitrarily large errors, so that their influence on the NLCG minimization procedure is negligible. In a next step, the difference errors within the thresholds are averaged, where the E^r average turned out to be below 1 percent. A minimum of 1 percent was enforced for these data. The average for E^q amounts to 2.26 %. Each complex datum (E_i^r,E_i^q) is then given a weight of $(w_i^r, w_i^q) = \left(\frac{1}{|E_i^r| e_i^r}, \frac{1}{|E_i^q| e_i^q}\right)$, where e_i^r and e_i^q are the individual percentage errors of the reciprocal measurements. If a value e_i^r or e_i^q is below its above mentioned minimum, e^r_{min} =1 % and e^q_{min}=2.26 %, then $e_i^r = e^r_{min}$ and/or $e_i^q = e^q_{min}$ is enforced.

Preliminary sensitivity study and synthetic test inversions

To quantify the resolution of the survey geometry given by the Rifle SIP data set, a 3-D sensitivity map is first generated by a model perturbation method. The underlying half-space model is given by the starting model which is used for the field data inversions shown below, and has the conductivities σ^r=0.027 S/m and σ^q=0.0001 S/m. These values were found through trial and error forward modeling to achieve a rough approximation of the baseline (t0) data along Array A. Figure 7 shows the data sensitivities, $S_j(\sigma^r)$ and $S_j(\sigma^q)$ (j=1,…,M), obtained by perturbing real and imaginary conductivity parameters of each of the shown FD model grid cells by a value of 10 percent and calculating the terms

$$S_j(\sigma^r) = \frac{\partial \mathbf{d}^p}{\partial \sigma_j^r} \approx \frac{\sum_{i=1}^{N} |d_i - d_i^0|}{\Delta \sigma_j^r} \quad \text{and} \quad S_j(\sigma^q) = \frac{\partial \mathbf{d}^p}{\partial \sigma_j^q} \approx \frac{\sum_{i=1}^{N} |d_i - d_i^0|}{\Delta \sigma_j^q} \quad . \qquad (13)$$

The summation terms denote the differences between the complex data d_i (i=1,…,N), generated from the perturbed model, and the corresponding unperturbed model response d_i^0. Note that the vector of the data simulations $\mathbf{d}^p$ comprises the electrode configurations of both profiles (Array A and B). The sensitivity map shows a quick decay of the sensitivities by roughly three orders of magnitude over the depth range of the local aquifer (down to 6.5 m), confirming the weak vertical resolution of this survey configuration. The lateral sensitivity decay between one array and the midpoint between Array A and B is less than 1.5 orders of magnitude. These strong sensitivity contrasts typically make structures tend to concentrate near the surface and in the vicinity of the profile line. Below we will demonstrate that the tendency to concentrate conductivity anomalies in areas of high sensitivity can be counteracted by the gradient weighting scheme introduced above.

We first carry out a comparative synthetic data inversion study between our 3-D algorithm and the 2-D algorithm employed in this work. The study intends to verify and illustrate the common trends in the images obtained from two fundamentally different inversion schemes, as we base our field data interpretation below on the common trends obtained from both solutions. For synthetic data creation, the field data electrode configuration as described above is simulated for one array configuration. Figure 8 (panels a and b) shows vertical cross sections of a simple 2-D model from which data is generated, and both model reproductions. Both solutions are given as resistivity magnitude and phase. The true model background is characterized by a resistivity magnitude of 50 $\Omega \cdot \mathrm{m}$ and a background phase of 5 mrad. The anomaly, extending infinitely along the y-direction, has the attributes 10 $\Omega \cdot \mathrm{m}$ and 25 mrad. To obtain independence from the underlying forward codes of each employed imaging algorithm, the synthetic data inverted by the 2-D solution is created from our 3-D FD code (using the forward solution represented by equation 5), and the synthetic data for the 3-D inversion was generated by the 2-D code. The finite element mesh of the 2-D method involves a 100×22 (x,z) mesh of rectangular elements, where 2079 elements form the actual inversion domain. The 3-D FD inversion domain involves a mesh of 80×40×20 (64000) unknowns. Panels c and d of Figure 8 show the (laterally invariant) gradient weighting function. The effect of this function is to counteract the natural sensitivity decay with depth by down-weighting high sensitivities in the shallow part of the inversion domain, thus enhancing the relatively weak sensitivities at depth. This function is realized by the

parameters a=0.001 and z_1=3.5 for $f_1(z)$ (equation 9) while $f_2(z) = 1$. Both images indicate the anomalous structure. The 2-D solution (e and f) approximates the shape of the true resistivity anomaly in a slightly better way, whereas the 3-D solution (g and h) reproduces a sharper image of the phase anomaly. The focusing effect of the gradient weighting scheme is demonstrated here by comparing with a 3-D solution generated without any weighting, shown in panels i and j. Here, the concentration of the anomalous resistivity magnitude near the surface as a result of the limited depth resolution is obvious. This distortion also leads to a weaker phase image.

A second synthetic study involves a more complex CR anomaly within a horizontally layered background. In this example we simulate measurements over a conductive complex resistivity anomaly, see Figure 9, using the same layout as given by Array A and B. The anomaly of enhanced conductivity is irregularly shaped within the y-z plane and extends for roughly 7 m along the x-axis. The x-axis is oriented parallel to Array A (at y=0 m) and Array B (at y=-6 m). Using a proper gradient weighting function, it is intended to demonstrate that reasonable resolution over a 3-D volume can still be obtained from the relatively sparse two-profile layout. The gradient weighting function with the 3-D weighting parameter distribution is illustrated in Figure 10. This function is constructed according to equation 11 and has lateral weighting, in addition to depth weighting. The chosen function parameters (x_a=3, x_b=13, y_a=-12, y_b=0, z_a=3.5, z_b=100, base weighting a=0.01) aim at a lateral focusing effect within a target area of interest while also damping high near-surface sensitivities. The focus area at x=13 m and y=-6 m is chosen assuming some prior knowledge about the extension of the anomalous conductivity distribution in Figure 9. The weighting effect is again demonstrated by first carrying out an inversion without gradient weighing (Figure 11) and comparing with the result employing weighting (Figure 12). The results show a greatly enhanced image for both real and imaginary conductivity. Although the result in Figure 12 has a relatively weak imaginary conductivity anomaly, the anomaly's location is clearly improved, compared to the non-weighting result. Despite the sparse data coverage, the focusing behavior of the gradient weighting helps to reproduce the true depth of the anomaly. We will employ a similar gradient weighting function in the following field data inversions.

Computational aspects of field data inversions

The computational FD grid size used for the environmental field data inversions is 132×87×149 (~1.7 million) cells. Each forward solution (including the adjoint solutions for gradient calculation) employed 125 CPUs of a parallel cluster with an Intel® Xeon™ architecture, CPU-speed 3.6 GHz. We used a total of 250 CPUs. The computing requirements for 10 3-D inversion iterations of the Rifle data, involving 52 transmitter activations, are 1404 BICG forward solutions, also including the adjoint solutions required for gradient calculation. The average BICG solution time was 9 seconds. This amounts to 3.5 hours total computing time. As noted above, the forward calculations involve the computationally more efficient solution of the Poisson equation. In comparison, solving the Maxwell equations in the forward problems, using a QMR solver, required an average solution time of 73 seconds, amounting to 24.3 hours of total computing time for 10 inversion iterations.

Inversion of data from a bioremediation monitoring experiment

In this study, we also employ the 2-D solution in order to compare with time-lapse trends observed in the 3-D solution. Vertical transects generated by the 3-D and 2-D solutions for resistivity magnitude and phase are shown in Figures 13 and 14, respectively. For a given recording time (t0 to t4), the 3-D images are produced from jointly inverting the data sets of both profiles, while the 2-D images are created by inverting each profile data set separately. Note that no measurements were made along Array B for the time t1. We obtained similar image solutions for the three different frequencies. Here, we present the results of the frequency f=1 Hz, because this data set showed the lowest overall data error in terms of the reciprocal measurements. For an image comparison, real and imaginary conductivities of the 3-D solution were converted to resistivity magnitude and phase values. We are primarily interested in comparing time-lapse resistivity magnitude and phase trends between both methods. Hence, we run all 3-D inversions for only ten inversion iterations. This avoids extreme overshoots when converting to resistivity and phase images, however results in worse data fits compared to the 2-D solutions. Table 2 lists the data fitting errors calculated from the starting model and the final images of each method. For a comparison made independent of each algorithm's internal data weighting scheme, the relative percentage error

$$error = \frac{\sum_{i=1}^{N} |d_i^{IO} - d_i^{IP}|}{\sum_{i=1}^{N} |d_i^{IO}|} \cdot 100 \ (\%) \tag{14}$$

is employed. This measure quantifies the absolute values of the unfitted part of the data as a percentage of the summed (and absolute) observation values. The stopping condition for the 2-D solution was given by a drop of the relative RMS error below the limit value of 0.02. All solutions achieve a satisfactory error level for the resistance magnitudes, while the phase data misfits are consistently larger, however can be decreased significantly with respect to the initial fits. The solutions are consistent in two aspects. First, the phase images below a depth of 2 m show relatively strong responses for the times from t0 to t2 and drop afterwards. Second, during t0 and t2 the phase responses are weaker below Array B than below Array A. While the resistivity magnitudes |ρ| remain relatively constant over the whole measurement time interval, the 3-D solution indicates a slight shift of the maximum of |ρ| towards Array B.

Interpretation of observed phase responses

The impact of acetate amendment, starting after time t0, on the SIP signals is interpreted here based on the common phase trends observed by using both image solutions. A particular outcome of the 2007 stimulation experiment was that, following acetate injection, the phase response of the sediments exhibited only modest changes relative to baseline conditions. As documented by the borehole data in Figure 15, although Fe(II) increased as a result of acetate amendment and the accompanying stimulation of iron reducing microorganisms, variations in Fe(II) concentration between the SIP acquisition time points were minimal. Measurements in wells D01-D04 indicated that a slight increase in phase magnitude observed along Array A during the t1 acquisition time accompanied an increase in fluid conductivity from 0.245 to 0.295 S/m, likely the result of the injection. Eleven days later (t2), both phase values and fluid conductivities remained elevated below Array A; at the time of this measurement, Fe(II) concentrations increased to their highest level in wells D02 and D03. Both 2-D and 3-D inverse solutions indicate decreasing phase responses after time t2. As acetate and bromide (data not shown) were eluted from the system following cessation of injection, Fe(II) concentrations decreased slightly, as did phase values measured during time points t3 and t4. The smaller

increases in both acetate and Fe(II) observed in wells D09-D12 as compared to D01-D04 corresponded to similarly small changes in the phase response along Array B at all time points. Increases in fluid conductivity were also smaller in well D09-D12, measurements showed a rise from approximately 0.24 to 0.26 S/m during the injection period.

The observed phase changes along Arrays A and B are in contrast to those previously reported for SIP experiments at the Rifle site, where large increases in phase magnitude were found to accompany acetate injection and the stimulation of iron and sulfate reducing microorganisms (Williams et al., 2009). A likely explanation involves the extent to which baseline Fe(II) concentrations were already elevated in the current study area, ranging from 50-100 μM prior to starting acetate injection. This is in contrast to areas of the Rifle site where SIP monitoring has previously been undertaken; there pre-injection Fe(II) concentrations were generally ≤10 μM. The difference is likely related to the presence of naturally elevated levels of subsurface microbial activity in the vicinity of Arrays A and B, which results from localized accumulation of buried organic carbon (e.g. wood, grass, roots, etc.) resulting in the accumulation of reduced aqueous and mineral species, such as Fe(II), FeS_2, and Fe_3O_4 (Qafoku et al., 2009). The presence of such material in the vicinity on Arrays A and B was confirmed during drilling of wells D02-D04, D11 and D12. As such, the modest increases in Fe(II) concentration above their initially elevated level likely minimized the Fe(II)-mediated phase effect.

Conclusions

We have successfully adapted a 3-D imaging algorithm for industrial-sized controlled-source EM data sets, as they are typical in oil and gas exploration, to treat surface SIP data sets. The algorithm's parallel architecture as well as its grid separation scheme make efficient use of today's scientific computing resources.

SIP measurements generated by frequencies above 10 Hz can contain significant inductive coupling effects. The mineral exploration synthetic case provided a demonstration of the effects on an imaging solution if not taken into account. EM coupling can be removed by appropriate preprocessing procedures. However, the success of such methods strongly depends on a reasonable knowledge of the background conductivity in an inversion, which might be time-

consuming to acquire as well. Therefore, we believe that solving the full Maxwell's equations in the forward modeling operator is important in interpreting high-frequency SIP data in a rigorous way. The rapid development in computing technology is a good indicator that the high computing costs for voluminous data sets reported here can be expected to decrease reasonably in the near future.

The SIP method has the potential of monitoring mineralogical and geochemical changes accompanying subsurface processes related to the remediation of mine wastes and bio-stimulated contaminant degradation in a minimally invasive way. A rigorous treatment in 3-D is important in order to treat arbitrary arrays of current and receiver electrodes over complex geological strata. Both the synthetic and field data studies have demonstrated that with adequate computing resources, our imaging solution, initially developed for large-scale hydrocarbon and geothermal energy exploration tasks, large amounts of (time-lapse) SIP data from 3-D surveys can be processed within reasonable timeframes.

The inversion of the field data and comparisons of the phase trends with an established 2-D solution indicate that our inversion approach is capable of yielding assessments of time varying phase and resistance magnitude signals collected during future IP and SIP monitoring applications. The ability to extend the inversion approach to three dimensions greatly extends the range of applications and previously reported results (Williams et al., 2009). The survey layout of the data treated here is characterized by a relatively low depth resolution, i.e. longer profile lengths would be necessary to increase depth resolution. However, we were able to increase the resolution properties by an appropriate gradient weighting scheme, which can be tailored to achieve lateral and/or vertical resolution enhancement. The synthetic studies on the Rifle data set show that the focusing effect of the gradient weighting scheme basically addresses the non-uniqueness issue of typically over-parameterized 3-D inverse problems.

Acknowledgments

Funding for this work was provided by the Environmental Remediation Science Program, Office of Biological and Environmental Research, U.S. Department of Energy (contract DE-AC02-05CH11231), Cooperative Agreement DE-FC02ER63446, and the Department of Energy, Office

of Basic Energy Sciences (contract DE-AC02-05CH11231). We thank Mike Wilkins, Hila Elifantz, Paula Mouser and Lucie N'Guessan for their assistance with field experiments. We further thank Andreas Kemna for providing the employed 2-D imaging code, and Adrián Flores-Orozco for help with using the 2-D code.

References

Anderson, R. T., H. A. Vrionis, I. Ortiz-Bernad, C. T. Resch, P. E. Long, R. Dayvault, K. Karp, S. Marutzky, D. R. Metzler, A. Peacock, D. C. White, M. Lowe, and D. R. Lovley, 2003, Stimulating the in situ activity of Geobacter species to remove uranium from the groundwater of a uranium-contaminated aquifer: Appl. Environ. Microb., 69, 5884-5891.

Börner, F. D., J. R. Schopper, and A. Weller, 1996, Evaluation of transport and storage properties in the soil and groundwater zone from induced polarization measurements: Geophysical Prospecting, 44, 583-601.

Commer, M., and G. A. Newman, 2008, New advances in three-dimensional controlled-source electromagnetic inversion, Geophysical Journal International, 172, 513-535.

Commer, M., G. A. Newman, J. J. Carazzone, T. A. Dickens, K. E. Green, L. A. Wahrmund, D. E. Willen, and J. Shiu, 2008, Massively-parallel electrical-conductivity imaging of hydrocarbons using the Blue Gene/L supercomputer, First Break, 26, 93-102.

Dey, A., and H. F. Morrison, 1973, Electromagnetic coupling in frequency and time-domain induced polarization surveys over a multilayered earth: Geophysics, 38, 380-405.

Flores-Orozco, A., A. Kemna, and E. Zimmermann, 2010, Data error quantification in spectral induced polarization imaging, submitted to Geophysics.

Hördt, A., R. Blaschek, A. Kemna, and N. Zisser, 2007, Hydraulic conductivity estimation from induced polarisation data at the field scale - the Krauthausen case history: Journal of Applied Geophysics, 62, 33-46.

Ingeman-Nielsen, T., and F. Baumgartner, 2006, Numerical modelling of complex resistivity effects on a homogenous half-space at low frequencies: Geophysical Prospecting, 54, 261-271.

Kemna, A., and A. Binley, 1996, Complex electrical resistivity tomography for contaminant plume delineation: Proc 3rd meeting Environmental and Engineering Geophysics, EEGS, Expanded Abstracts, 151-154.

Kemna, A., 2000, Tomographic inversion of complex resistivity, theory and application: Der andere Verlag, Bochum, Germany.

Kemna, A., A. Binley, A. Ramirez, and W. Daily, 2000, Complex resistivity tomography for environmental applications: Chem. Eng. J., 77, 11-18.

Li, Y., and D. W. Oldenburg, 1998, 3D inversion of gravity data, Geophysics, 63, 109–119.

Loke, M. H., J. E. Chambers, and R. D. Ogilvy, 2006, Inversion of 2D spectral induced polarization imaging data: Geophysical Prospecting, 54, 287-301.

Madden, T. R., and T. Cantwell, 1967, Induced polarization, a review, *in* Mining Geophysics Vol. 2, Society of Exploration Geophysicists, Tulsa, Oklahoma, 373-400.

Newman, G. A., G. W. Hohmann, and W. L. Anderson, 1986, Transient electromagnetic response of a three-dimensional body in a layered earth: Geophysics, 51, 1608-1627.

Newman, G. A., and G. M. Hoversten, 2000, Solution strategies for two- and three-dimensional electromagnetic inverse problems: Inverse problems, 16, 1357-1375.

Newman, G. A., and D. L. Alumbaugh, 2002, Three-dimensional induction logging problems, Part 2: A finite-difference solution: Geophysics, 67, 484-491.

Newman, G. A., M. Commer, and J. J. Carazzone, 2010, Imaging controlled-source electromagnetic data in the presence of electrical anisotropy: Geophysics, 75, F51-F61.

Ntarlagiannis, D., Williams, K. H., Slater, L. D., and Hubbard, S. S., 2005, Low-frequency electrical response to microbial induced sulfide precipitation: J. Geophys. Res., 110, G02009, doi:10.1029/2005JG000024.

Oldenburg, D. W., and Y. Li, 1994, Inversion of induced polarization data: Geophysics, 59, 1327-1341.

Pelton, W. H., S. H. Ward, P. G. Hallof, W. R. Sill, and P. H. Nelson, 1978, Mineral discrimination and removal of inductive coupling with multifrequency IP: Geophysics, 43, 588, DOI:10.1190/1.1440839

Qafoku, N. P., R. K. Kukkadapu, J. P. McKinley, B. W. Arey, S. D. Kelly, C. M. Wang, C. T. Resch, and P. E. Long, 2009, Uranium in Framboidal Pyrite from a Naturally Bioreduced Alluvial Sediment: Environ. Sci. Technol., 43, 8528-8534.

Routh, P. S., and D. W. Oldenburg, 2001, EM coupling in frequency-domain induced polarization data: a method for removal, Geophysical Journal International 145, 59–76.

Shi, W., W. Rodi, and F. Morgan, 1998, 3-D induced polarization inversion using complex electrical resistivities: SAGEEP Proceedings, 785-794.

Slater, L., and Lesmes, D. P., Electrical-hydraulic relationships observed for unconsolidated sediments, Water Resour. Res., 38 , 1213, 2002.

Song, L., 1984, A new IP decoupling scheme, Exploration Geophysics, 15, 99–112.

Sumi, F., 1959, Geophysical exploration in mining by induced polarization: Geophysical prospecting, 7, 300-310.

Ulrich, C., and L. D. Slater, 2004, Induced polarization measurements on unsaturated, unconsolidated sands: Geophysics, 69, 762-771.

Van Voorhis, G. D., P. H. Nelson, and T. L. Drake, 1973, Complex resistivity spectra of porphyry copper mineralization: Geophysics, 38, 49–60.

Vacquier, V., C. R. Holmes, P. R. Kintzinger, and M. Lavergue, 1957, Prospecting for groundwater by induced electric polarization: Geophysics, 22, 660-687.

Weller, A., W. Frangos, and M. Seichter, 2000, Three-dimensional inversion of induced polarization data from simulated waste: Journal of Applied Geophysics, 44, 67-83.

Williams, K. H., Ntarlagiannis, D., Slater, L. D., Dohnalkova, A., Hubbard, S. S., and Banfield, J. F., 2005, Geophysical imaging of stimulated microbial biomineralization: Environ. Sci. Technol., 39, 7592-7600.

Williams, K. H., A. Kemna, M. J. Wilkins, J. Druhan, E. Arntzen, A. L. N'Guessan, P. E. Long, S. S. Hubbard, and J. F. Banfield, 2009, Geophysical monitoring of coupled microbial and geochemical processes during stimulated subsurface bioremediation: Environ. Sci. Technol., 43, 6717-6723.

Wynn, J. C., and K. L. Zonge, 1975, Electromagnetic coupling, its intrinsic value, its removal and the cultural coupling problem, Geophysics, 40, 831–850.

Yang, X., D. LaBrecque, G. Morelli, W. Daily, and A. Ramirez, 2000, Three-dimensional complex resistivity tomography, SAGEEP Proceedings, 897-907.

Appendix

3-D inverse modeling for complex anisotropic conductivity

The solutions of the forward problems given by equations 2 and 5 are accelerated by defining FD meshes specifically adapted to spatial grid sampling requirements, given by the SIP survey geometries and source excitation frequencies. This allows the construction of generally coarser and smaller (in terms of their spatial extent) FD meshes than given by the usually larger common model grid. The modeling grid defines the inversion parameters, i.e. the real and imaginary conductivities assigned to each grid cell. In the following the notation $\sigma^{r,q}$ means that a given equation holds for either σ^{r} or σ^{q}, and a similar notation will be used to denote one of the three directional conductivities along the Cartesian coordinates *x*, *y*, or *z*. The grid separation involves

proper grid mapping schemes between the edge space on which the electric field **E** is sampled (Ω_S) and the node space given by the common model grid (Ω_M) (Commer and Newman, 2008). The conductivity averaging functions for calculating the directional edge conductivities on the Cartesian FD grid Ω_S from the cell conductivities $\sigma^{r,q}$ on Ω_M are written in a general form as

$$\sigma_{e_x}^{r,q}(\sigma^{r,q}) = \left[\int\left(\frac{1}{V}\int_V \sigma^{r,q}dV\right)^{-1} dx\right]^{-1} dX \tag{A-1}$$

$$\sigma_{e_y}^{r,q}(\sigma^{r,q}) = \left[\int\left(\frac{1}{V}\int_V \sigma^{r,q}dV\right)^{-1} dy\right]^{-1} dY \tag{A-2}$$

$$\sigma_{e_z}^{r,q}(\sigma^{r,q}) = \left[\int\left(\frac{1}{V}\int_V \sigma^{r,q}dV\right)^{-1} dz\right]^{-1} dZ \tag{A-3}$$

Here $\sigma_{e_x}^{r,q}$, $\sigma_{e_y}^{r,q}$, and $\sigma_{e_z}^{r,q}$ are the directional edge conductivities on Ω_S, and dX, dY, and dZ are their corresponding edge lengths. The conductivity tensor given above below equation 1 then reads

$$\sigma^* = \begin{pmatrix} \sigma_{e_x}^{r} + i\sigma_{e_x}^{q} & 0 & 0 \\ 0 & \sigma_{e_y}^{r} + i\sigma_{e_y}^{q} & 0 \\ 0 & 0 & \sigma_{e_z}^{r} + i\sigma_{e_z}^{q} \end{pmatrix}.$$

Note that the edge lengths are given by the distances between neighboring nodes on a Cartesian FD grid. In principal, the edge conductivity represents a harmonic average of a series of parallel circuits. In equations A-1 to A-3, the term in brackets represents a serial connection of parallel circuits, where the outer integration (dX, dY, or dZ) is carried out along the edge length. The integration section along dx, dy, or dz in turn is comprised as a parallel circuit of all cell conductivities $\sigma^{r,q}$ which overlap the parallel circuit's total integration volume V (with dV being the overlapping cell volume). For example, for the x-coordinate V is given by $dx \cdot S$ where S is an integration area in the yz-plane defining the volume $dX \cdot S$ over which the edge conductivity $\sigma_{e_x}^{r,q}$ is defined.

To formulate the general case of inverting for complex and anisotropic conductivity distributions we redefine the model parameter vector **m**, now comprised of $6M$ components,

$$\mathbf{m} = (\sigma_x^r, \sigma_y^r, \sigma_z^r, \sigma_x^q, \sigma_y^q, \sigma_z^q)^T.$$

Recall that M is the number of FD grid cells on the model grid Ω_M defining the inversion parameter space (usually a subdomain of Ω_M). Here one entry $\sigma_{x,y,z}^{r,q}$ represents a vector with M components. It has been shown in recent works (Commer and Newman, 2008; Newman et al., 2010) how the gradient of the objective functional (equation 6) is related to **m**. In summary, one has the data and model components,

$$\nabla\phi = \nabla\phi_d + \nabla\phi_m$$

where calculation of the model term is straightforward

$$\nabla\phi_m = \sum_{i=1}^{6} \lambda_i \mathbf{W}_i^* \mathbf{W}_i \mathbf{m}_i$$

In this general case, i=1,…,6 selects one of the six vectors $\mathbf{m}_i = \sigma_{x,y,z}^{r,q}$ which comprise **m**. The term $\nabla\phi_d$ involves the derivative of the data prediction vector $\mathbf{d}^p$ with respect to **m**, which further requires the Jacobian and hence the derivative of the forward modeling operator (equation 2). This leads to (Newman et al., 2010)

$$\frac{\partial \mathbf{E}}{\delta\sigma_{x,y,z}^{r,q}} = \mathbf{K}^{-1}\left(\frac{\partial \mathbf{S}}{\partial\sigma_{x,y,z}^{r,q}} - \frac{\partial \mathbf{K}}{\partial\sigma_{x,y,z}^{r,q}}\mathbf{E}\right).$$

Since **E**, **S**, and **K** are defined on the edge space Ω_S, this term involves application of the chain rule,

$$\partial \text{"E"} /(\partial\sigma_1(x,y,z)^{\uparrow}(r,q)) = \text{"K"}^{\uparrow}(-1)\ (\Sigma_1(l=1)^{\uparrow}(P_{\perp\theta}) \quad [\partial \text{"S"} /(\partial\sigma_1(x,y,z)^{\uparrow}(r,q))\ \ (\partial\sigma_{\perp}(x,y,z)^{\uparrow}(r,q))/($$

The term $P_\theta = P_\theta\left(\sigma_{x,y,z}^{r,q}\right)$ involves a transposition of the linear grid mapping operators given by equations A-1 – A-3. In principle, for a given cell parameter $\sigma_{x,y,z}^{r,q}$, the operator $P_\theta\left(\sigma_{x,y,z}^{r,q}\right)$ selects all edge conductivities $\sigma_{\theta\,x,y,z}^{r,q}$ which have a contribution from $\sigma_{x,y,z}^{r,q}$ through application of the chain rule to the averaging schemes in equations A-1 – A-3. For illustrative examples of a

discrete formulation of equations A-1 – A-3 and the corresponding derivative terms $\frac{\partial \sigma_{x,y,z}^{r,q}}{\partial \sigma_{\varphi x,y,z}^{r,q}}$, the reader is referred to Commer and Newman (2008).

Tables and Figures

Measurement time	Array A	Array B
t0	08-06-2007	08-07-2007
t1	08-18-2007	-
t2	08-29-2007	08-28-2007
t3	09-14-2007	09-14-2007
t4	11-02-2007	11-01-2007

Table 1: Acquisition dates for surface SIP data collected in conjunction with acetate amendment at the Rifle Integrated Field Research Challenge site near Rifle, Colorado. Measurement time 't0' refers to baseline data collected prior to starting acetate injection, which began 08-08-2007 and ended 09-08-2007.

	t0	t1	t2	t3	t4
3-D starting model	52.43 / 37.96	58.24 / 42.16	48.63 / 39.82	46.77 / 28.07	44.48 / 18.66
3-D final model	6.76 / 18.28	5.75 / 12.11	7.22 / 17.82	7.32 / 18.41	5.62 / 13.68
2-D starting model	83.83 / 100	85.85 / 100	83.34 / 100	82.83 / 100	81.45 / 100
2-D final model	0.57 / 10.10	1.76 / 29.53	0.58 / 9.28	1.23 / 9.29	0.82 / 6.66

Table 2: Fitting errors for the data components resistance magnitude $|R|$ and phase. Errors are given in percent, using equation 11. The entries are given by the pairs $|R|$ / phase. Compared are initial and final data fits between the 2-D and 3-D solutions. Note that before error calculation real and imaginary electric field data obtained from the 3-D solution were converted to $|R|$ / phase values. Also, the 2-D solution starts with a zero phase guess, hence the initial phase fitting error is 100 percent.

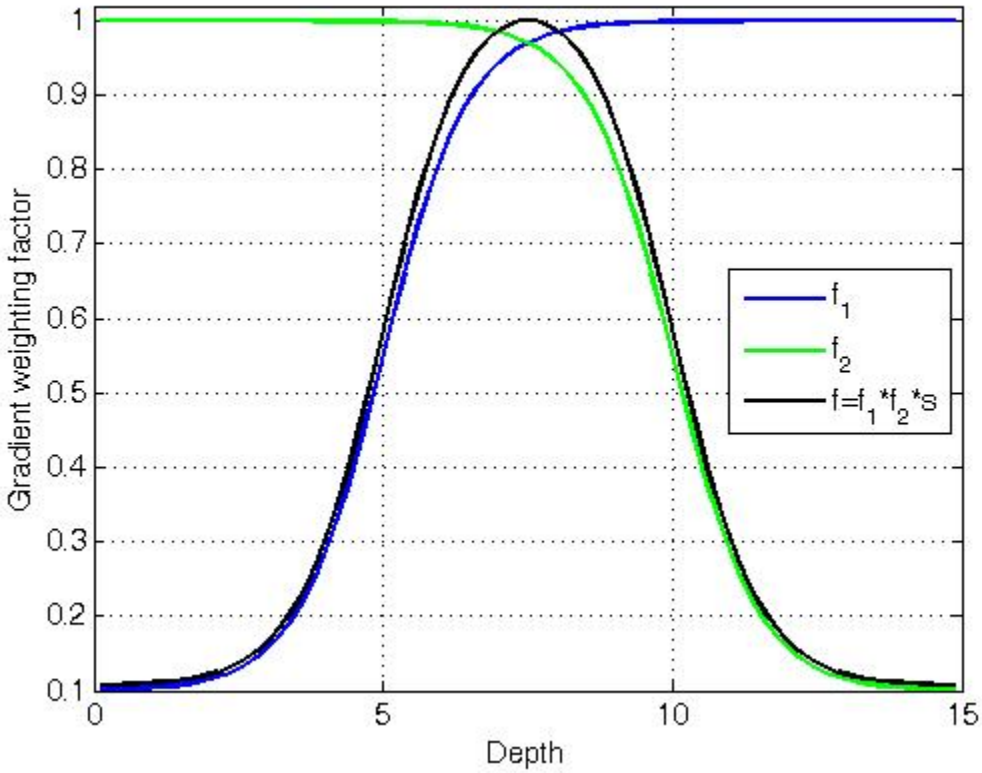

Figure 1: Illustration of gradient weighting functions. The exponential function behavior with depth is plotted for two gradient weighting functions, f_1 and f_2 (equations 9 and 10), and their combination f. Here, the function parameter is a=0.1 for both f_1 and $f2$. To obtain a lateral focusing behavior, the combined function f can be applied the same way to a horizontal coordinate.

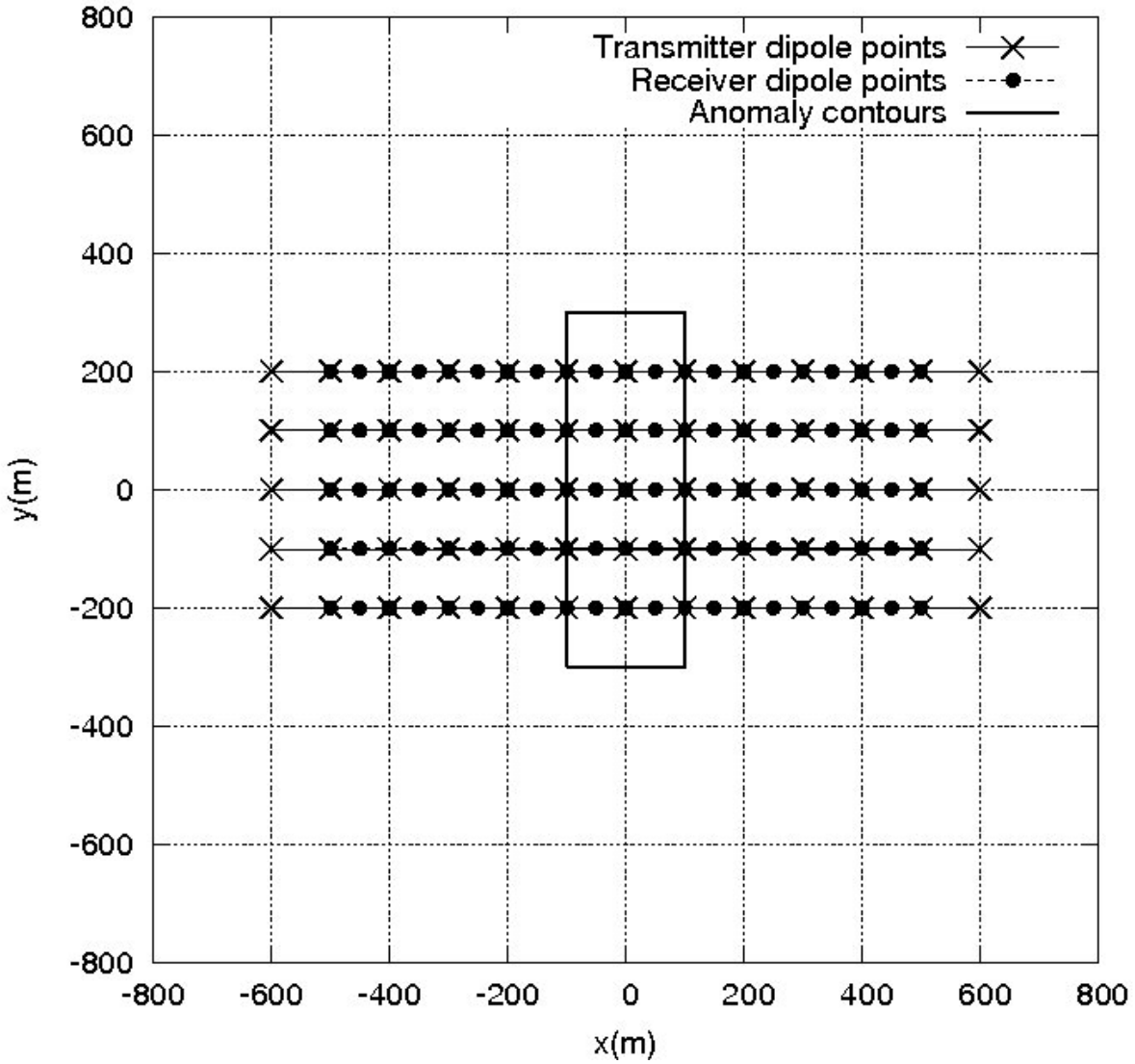
Transmitter dipole points
Receiver dipole points
Anomaly contours
800
600
400
200
0
-200
-400
-600
-800
y(m)
-800
-600
-400
-200
0
200
400
600
800
x(m)

Figure 2: Survey setup for the simulation of a mining exploration example. The shown anomaly contours are from a polarizable body with a depth extension from 100 to 200 m.

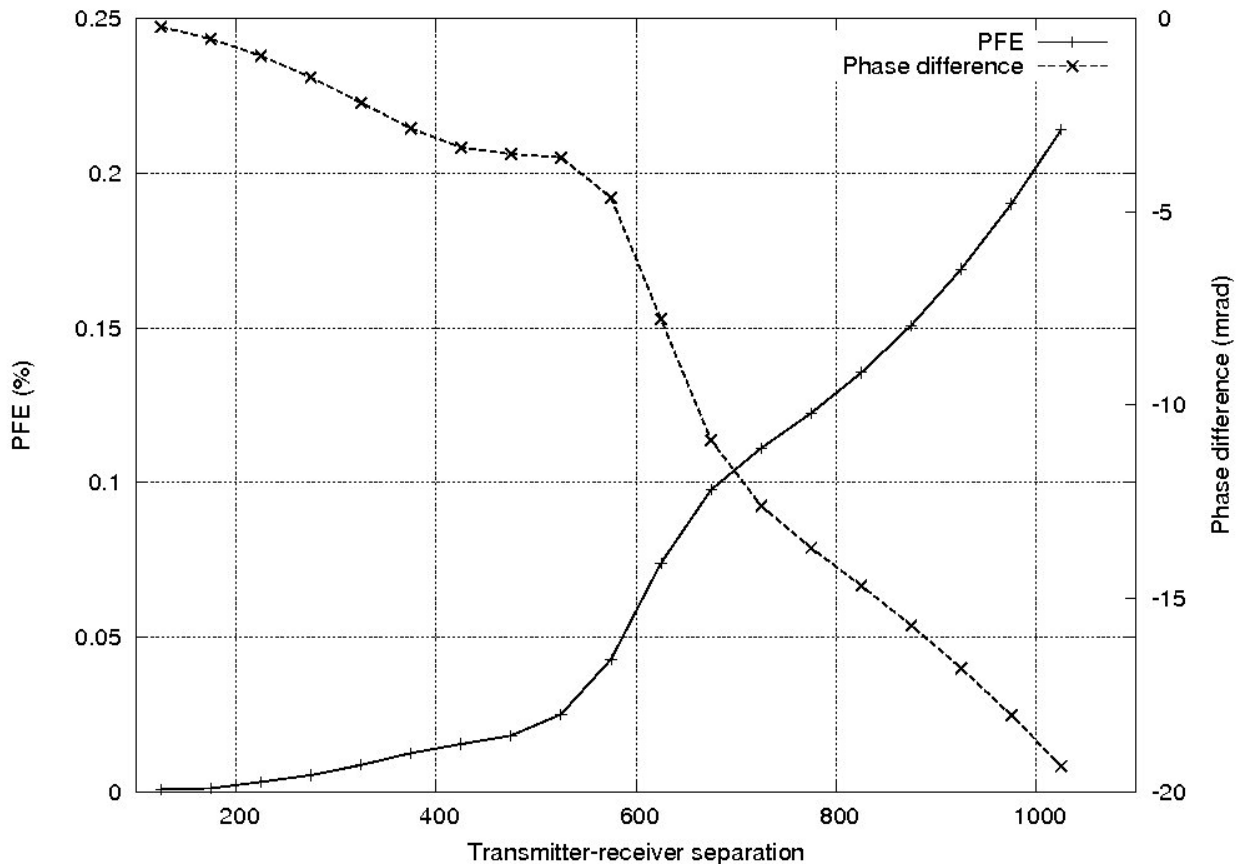

Figure 3: Quantification of the degree of EM coupling calculated for the true model of the mineral deposit example. Percent frequency effect (PFE) and phase difference ($\Delta\theta$) are computed from the direct current and alternating current mutual resistances, Z^{dc} and Z^{em}.

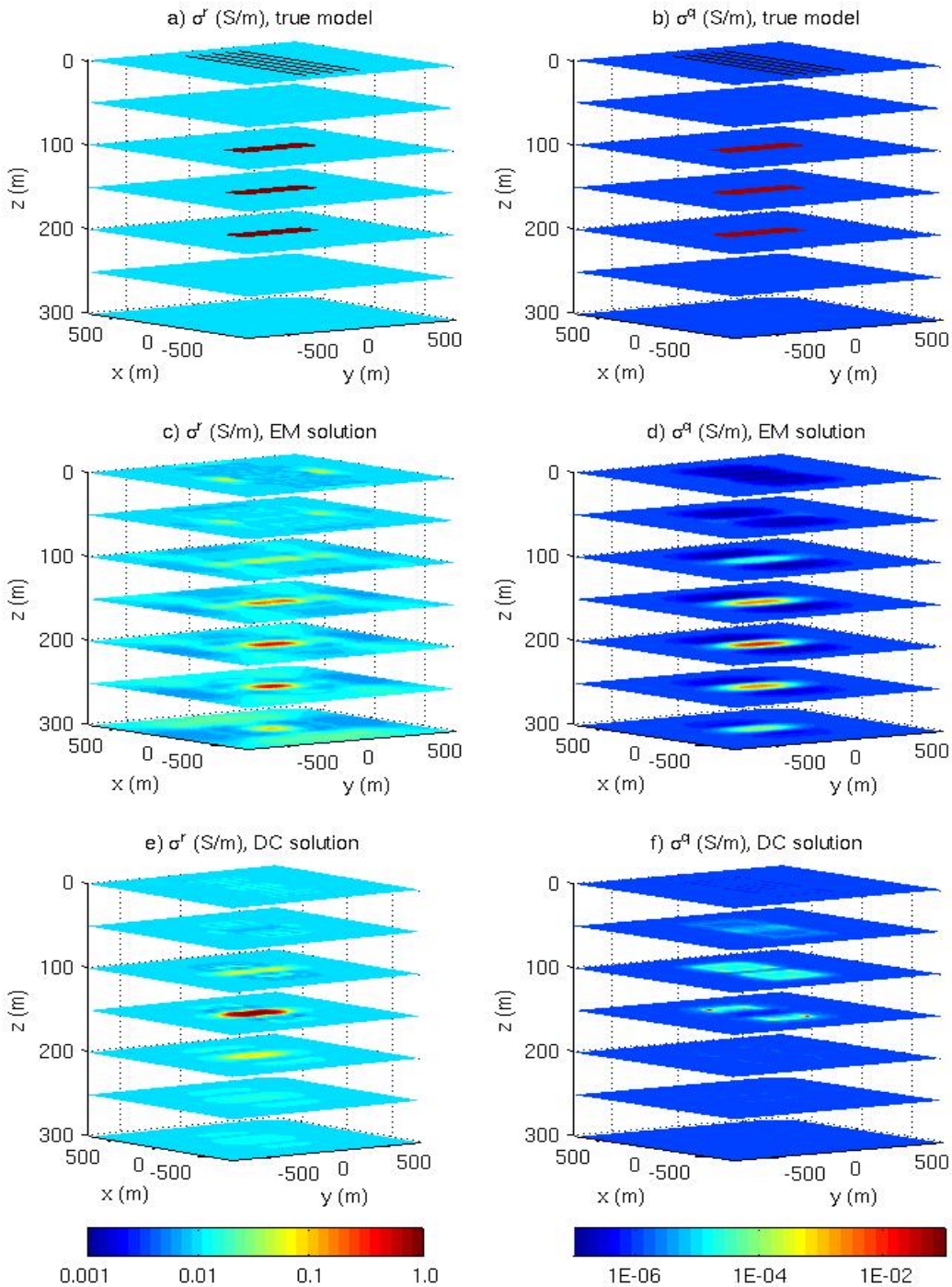

Figure 4: Sections of the model simulating a mineral exploration SIP survey. The model grid simulating the earth below the surface (z=0 m) contains 167×167×84 FD grid cells with a minimum grid interval of 12.5 m. The true model has $\sigma^r = 1$ S/m (a) and $\sigma^q = 0.05$ S/m (b). Also shown in a and b are the five receiver profiles at z=0 m. Figures c and d show the imaging

result obtained from using the EM forward modeling operator, whereas e and f are obtained from using the DC formulation.

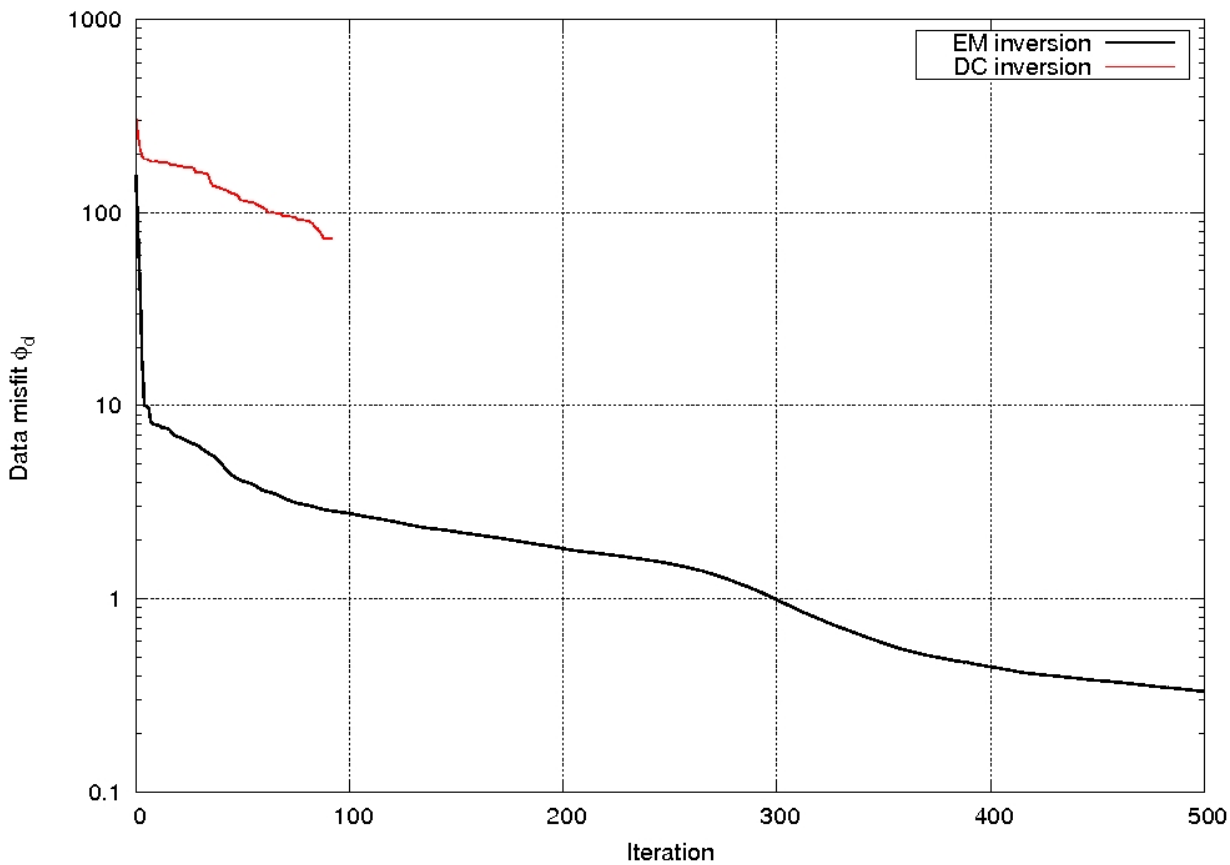

Figure 5: Data component ϕ_d of the objective function for the imaging results shown in Figure 4. The inversion run using the DC forward operator failed in the NLCG line-search procedure after 92 inversion iterations.

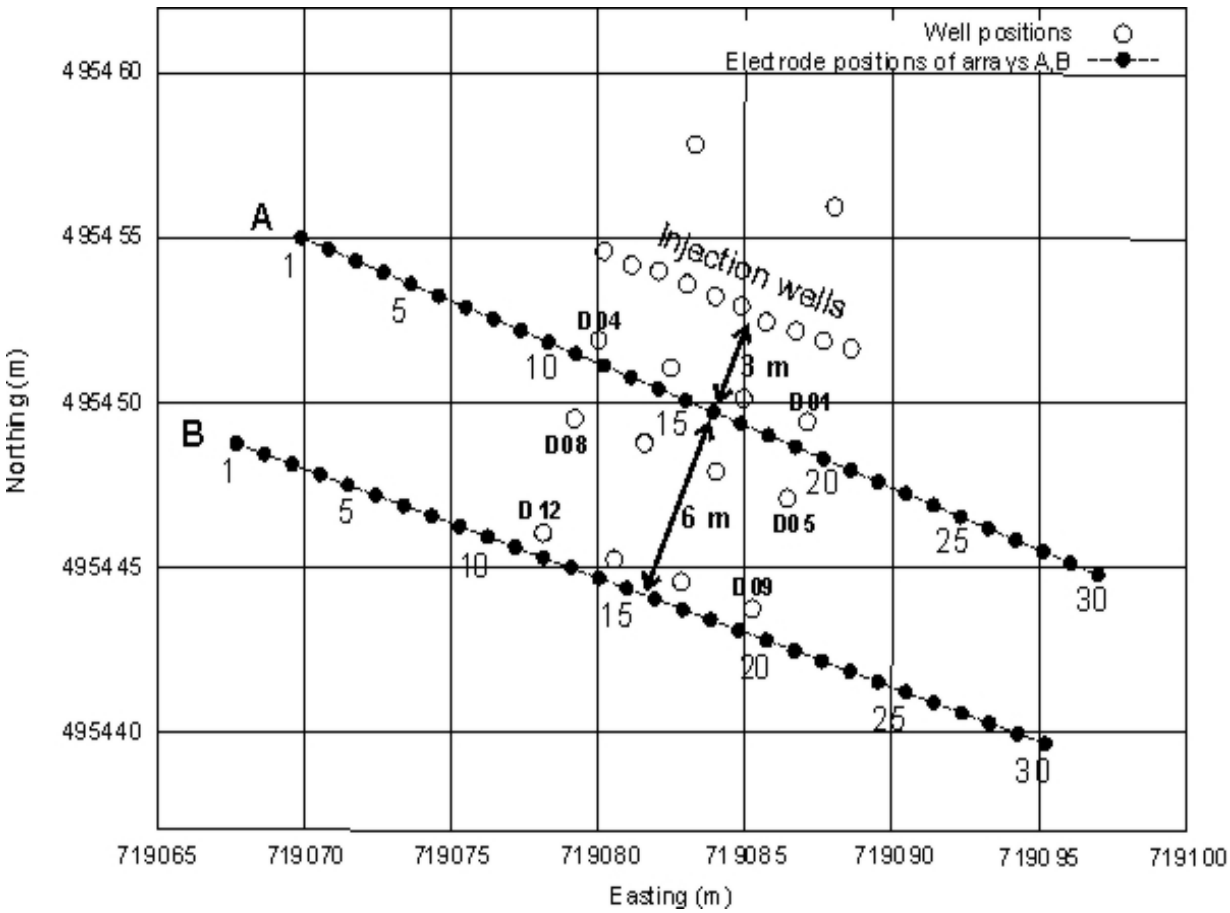

Figure 6: Layout of SIP profiles and injection and observation wells at the environmental remediation monitoring site at Rifle (Colorado). The profile length of Array A and B is 29 m.

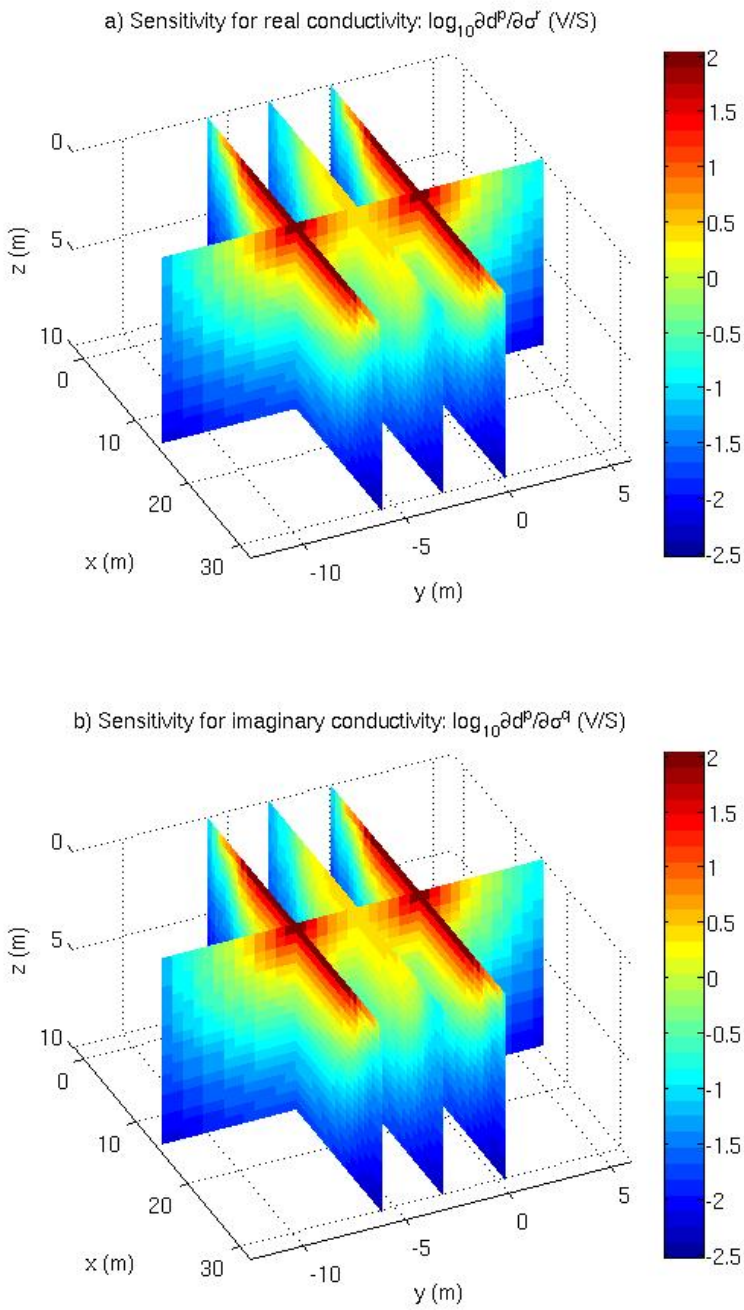

Figure 7: Sensitivity map obtained from a perturbation approach. The real and imaginary conductivity values of the starting model used for the Rifle data inversion were perturbed by a value of 10 %. The *x*-coordinate is parallel to the arrays A and B, and the *y*-coordinate is roughly coincident with groundwater flow which is towards the negative direction. Array A is at y=0 m and B is at y=-6 m.

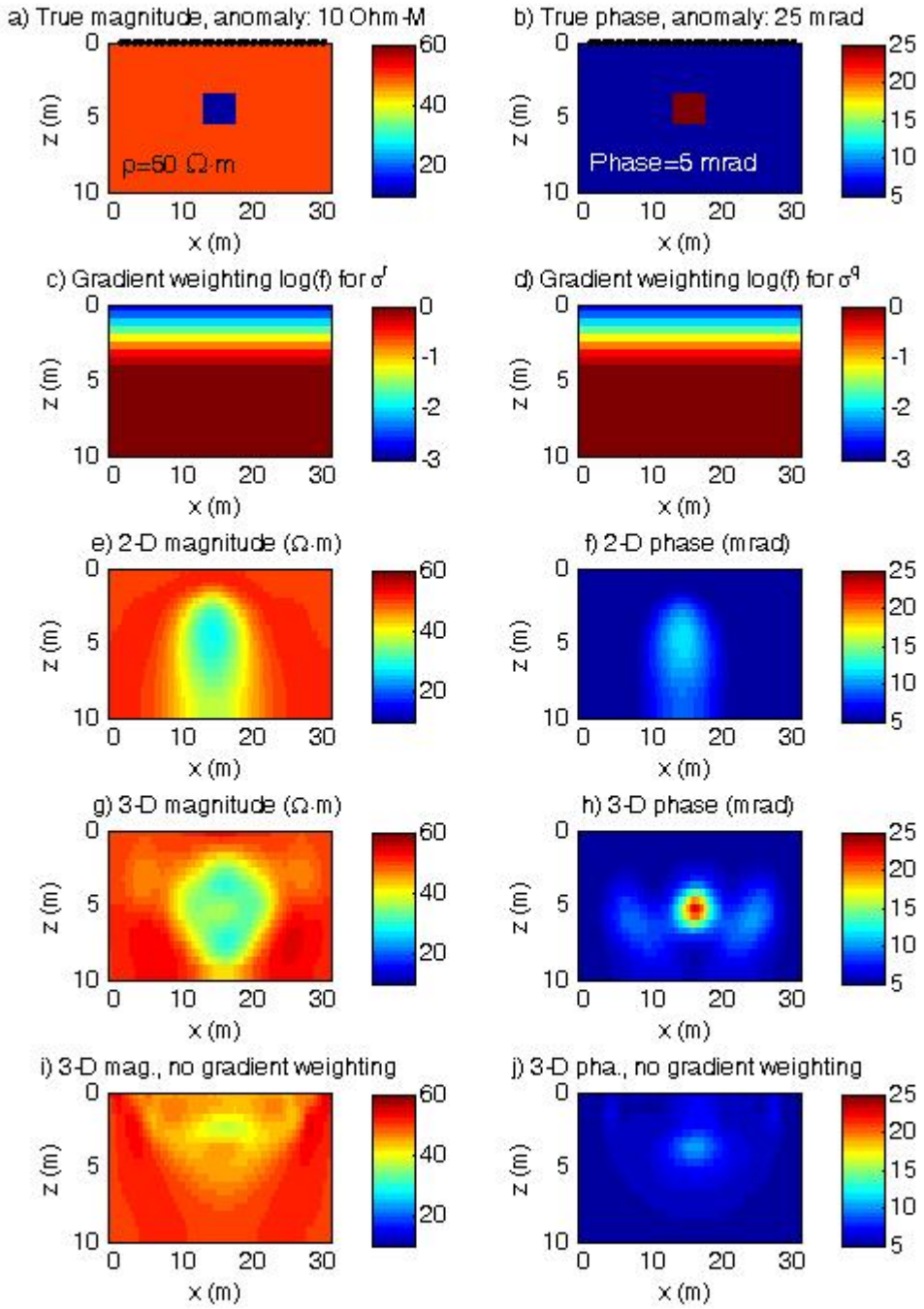

Figure 8: Synthetic data inversion results for a 2-D model anomaly using one profile of the Rifle survey (environmental remediation monitoring experiment). Left panels correspond to resistivity magnitude, right panels correspond to phase. Our 3-D solutions were converted to resistivity

magnitude and phase. (a) and (b) show the true model anomaly within a homogeneous half-space, and the profile layout at z=0 m. (c) and (d) illustrate the (vertical) gradient weighting function of our 3-D solution applied to the gradients of σ^r and σ^q, respectively. (e) and (f) show a 2-D inversion result obtained from a finite-element algorithm (Kemna, 2000). Panels (g) and (h) show our 3-D solution using the vertical gradient weighting. The solutions in panels (i) and (j) were obtained without gradient weighting.

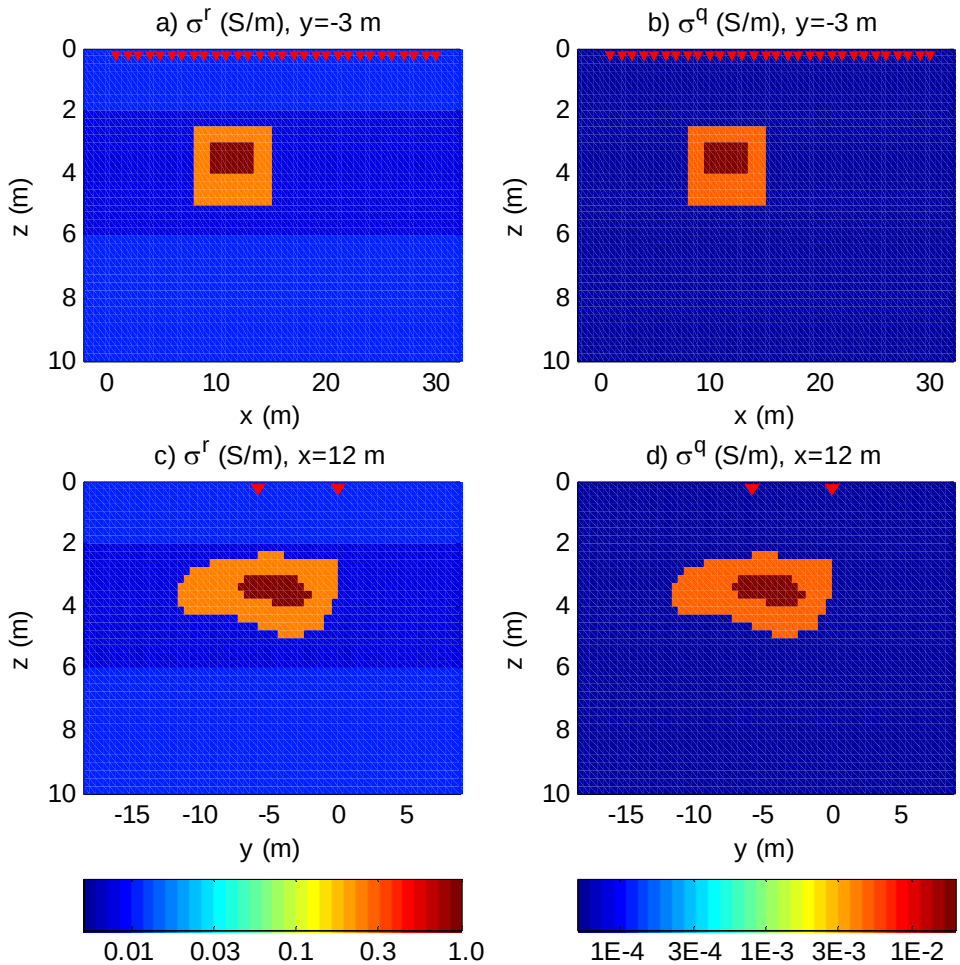

Figure 9: 3-D model used for generating synthetic data simulating a survey at the environmental remediation monitoring field site at Rifle. The complex conductivity anomaly has maximum values of σ^r=1 S/m and σ^q=0.02 S/m. The background real conductivity is given by three layers with 0.01 S/m (z=0-2 m), 0.0077 S/m (z=2-6 m), and 0.01 S/m (z>6 m). The background imaginary half-space conductivity is $\sigma^q=5\cdot10^{-5}$ S/m. The red symbols indicate the two-profile layout of the Rifle data.

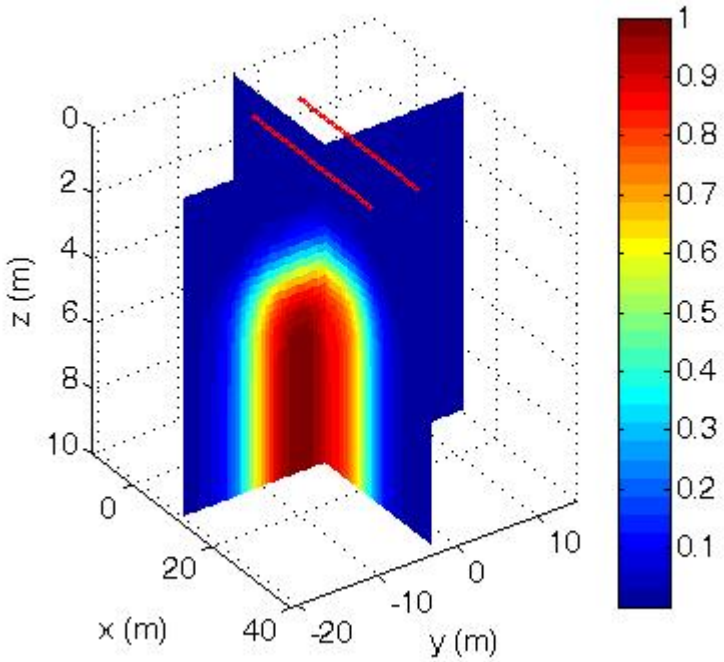

Figure 10: Illustration of 3-D gradient weighting function used for inverting synthetic data of the environmental remediation monitoring field site. The red lines at z=0 m indicate the positions of Arrays A and B at y=-6 m and y=0 m. The weighing function employed here aims at damping high near-surface sensitivities. Moreover, a laterally focusing behavior is enforced along both horizontal axes in order to account for the limited lateral resolution of the two profiles.

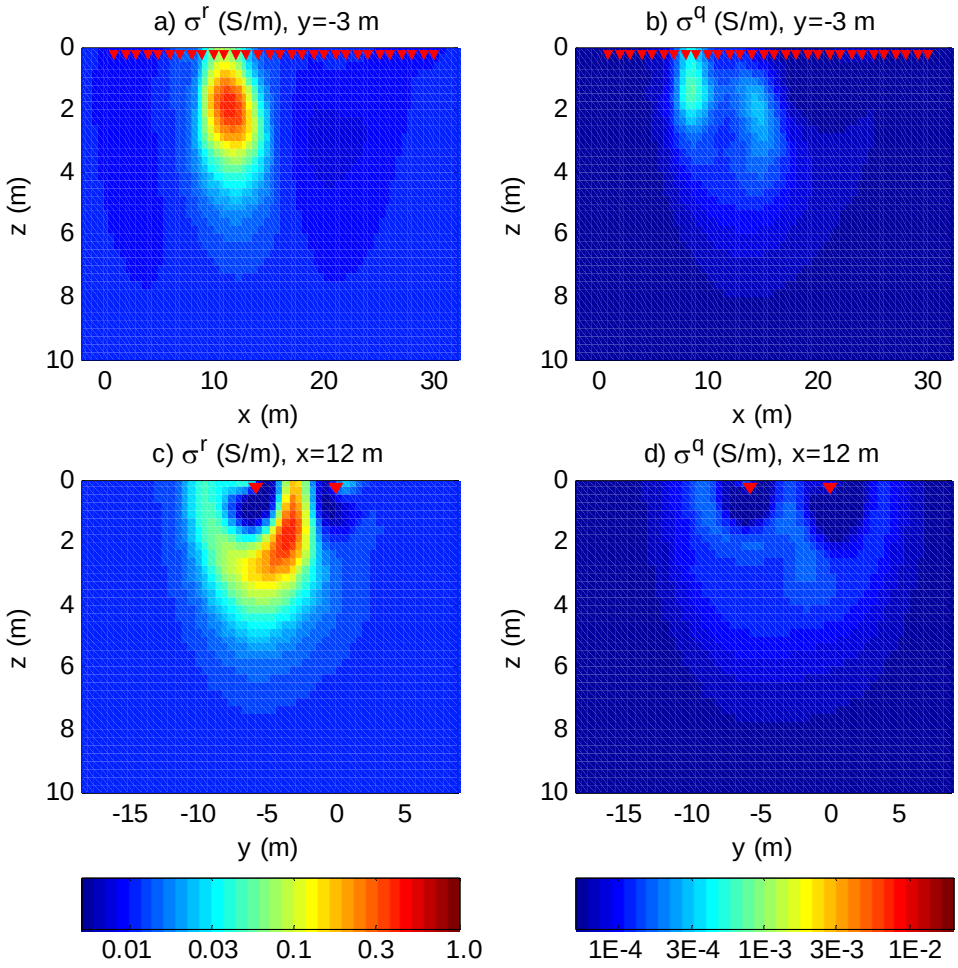

Figure 11: Images for real and imaginary conductivity obtained from inverting the synthetic Rifle data. Here, no gradient weighting was applied.

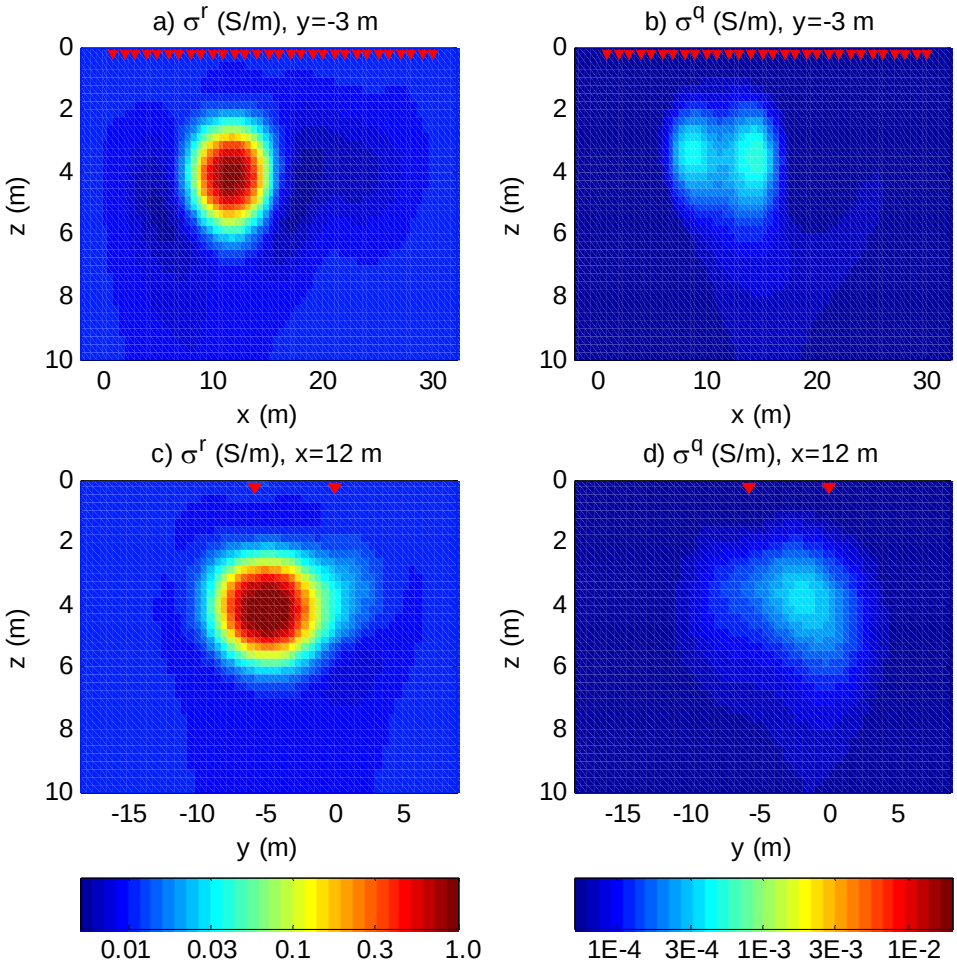

Figure 12: Images for real and imaginary conductivity obtained from inverting the synthetic Rifle data. Here, gradient weighting as depicted above in Figure 10 was applied.

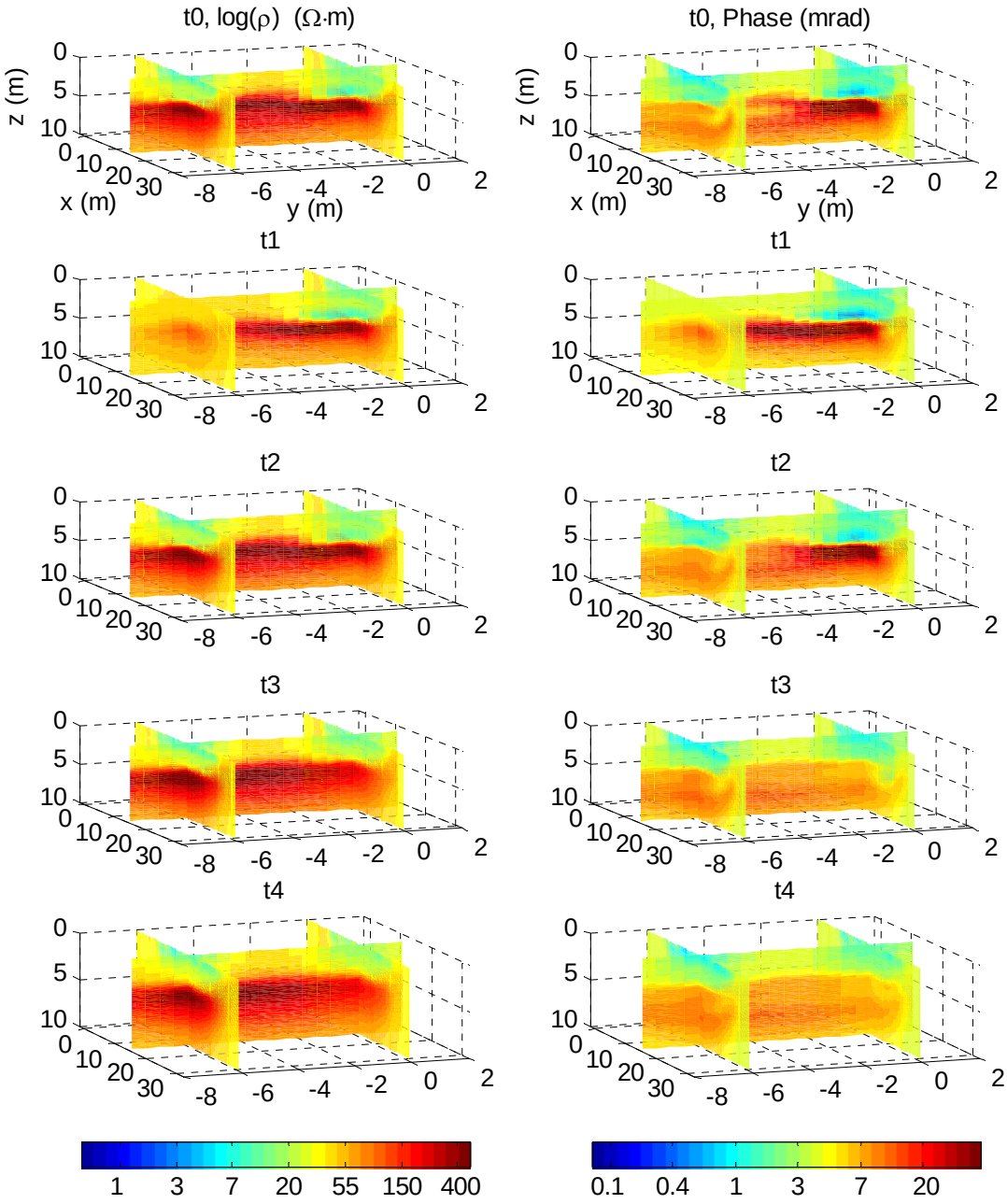

Figure 13: 3-D inversion result of SIP data from a bioremediation monitoring experiment. Shown are amplitudes and phases calculated from real and imaginary conductivity images.

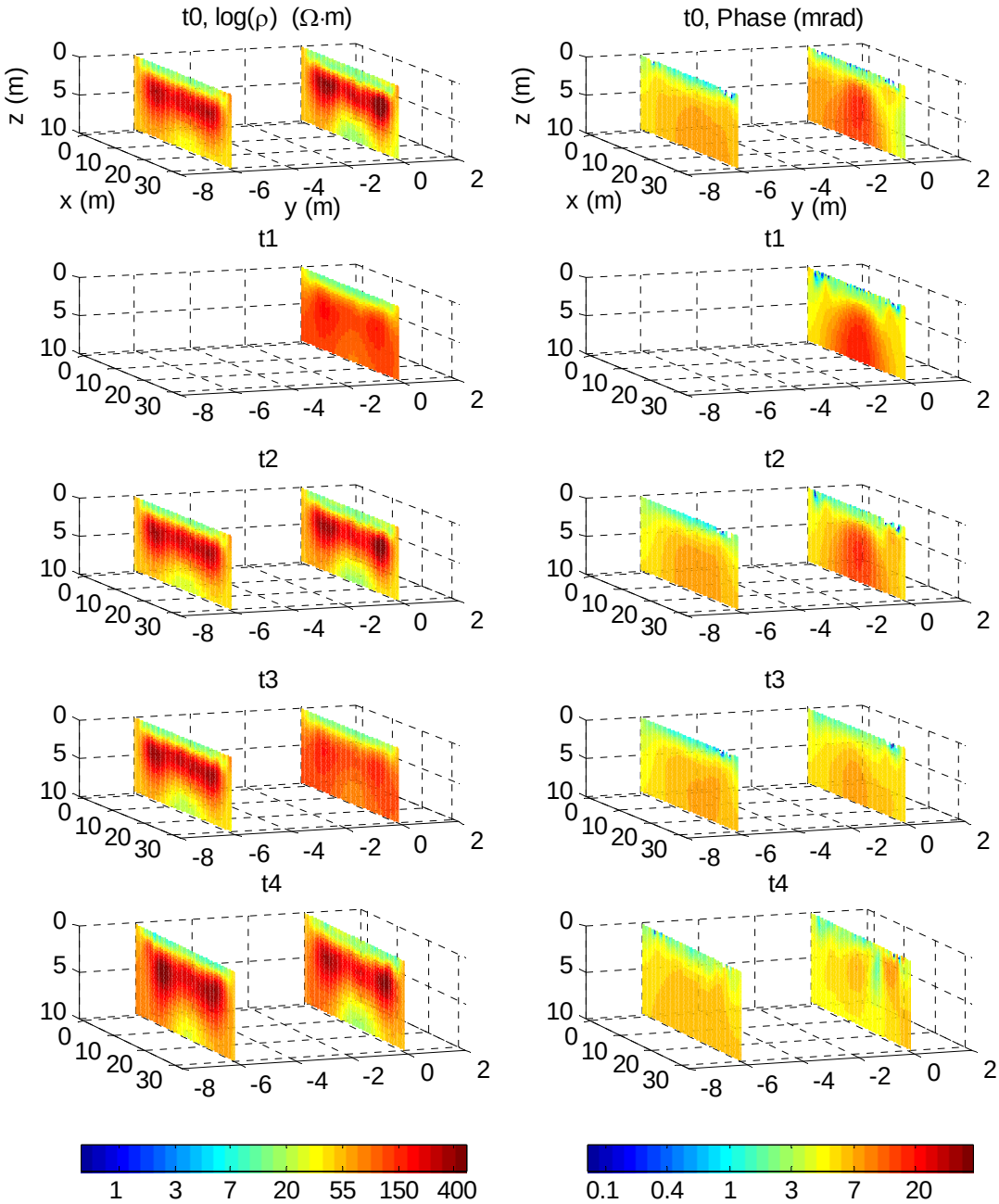

Figure 14: 2-D inversion result of SIP data from a bioremediation monitoring experiment. Each data set corresponding to Array A and Array B was inverted separately.

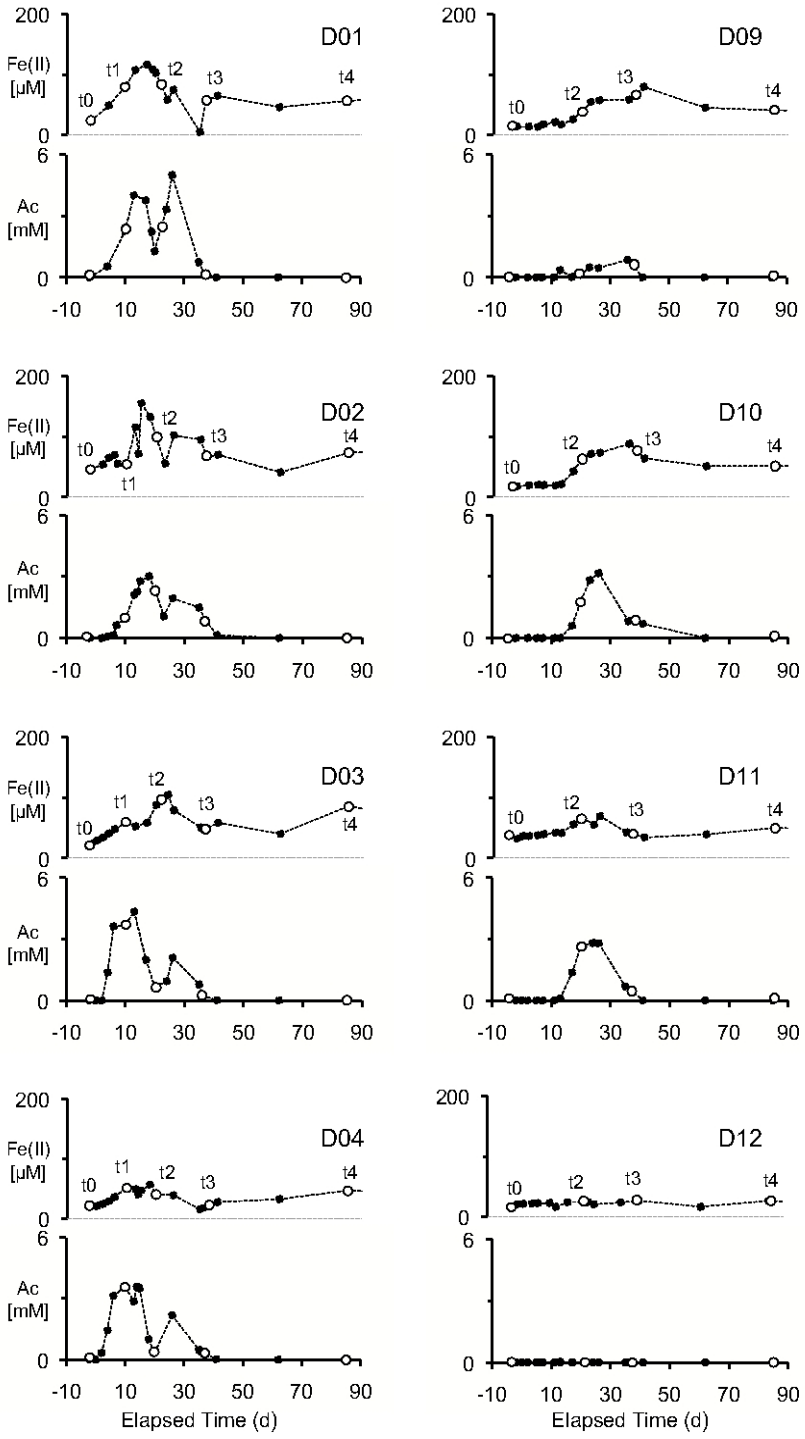

Figure 15: Spatiotemporal change in groundwater Fe(II) and acetate molar concentrations following acetate injection; elapsed time refers to the start of acetate injection. Data from down-gradient wells D01-D04 and D09-D12 were chosen, as they are located along transects Array A and B, respectively (Figure 6). Sample points corresponding to the SIP acquisition dates specified in Table 1 (e.g. t0, t1, t2, etc.) are indicated by open symbols.

DISCLAIMER

This document was prepared as an account of work sponsored by the United States Government. While this document is believed to contain correct information, neither the United States Government nor any agency thereof, nor The Regents of the University of California, nor any of their employees, makes any warranty, express or implied, or assumes any legal responsibility for the accuracy, completeness, or usefulness of any information, apparatus, product, or process disclosed, or represents that its use would not infringe privately owned rights. Reference herein to any specific commercial product, process, or service by its trade name, trademark, manufacturer, or otherwise, does not necessarily constitute or imply its endorsement, recommendation, or favoring by the United States Government or any agency thereof, or The Regents of the University of California. The views and opinions of authors expressed herein do not necessarily state or reflect those of the United States Government or any agency thereof or The Regents of the University of California.

Ernest Orlando Lawrence Berkeley National Laboratory is an equal opportunity employer.